nature neuroscience

Article

https://doi.org/10.1038/s41593-026-02339-4

Voltage dynamics of cortical dendrites in vivo

Received: 28 April 2025

Accepted: 8 May 2026

Published online: 19 June 2026

Check for updates

J. David Wong-Campos[1,2,5], Pojeong Park[1,3,5], Byung Hun Lee[1,5], Hunter C. Davis[1], Yitong Qi[1], He Tian[1], Daniel G. Itkis[1], Doyeon Kim[1], Jonathan B. Grimm[2], Sarah E. Plutkis[2], Luke D. Lavis[2] & Adam E. Cohen[1,4]

Voltage dynamics in dendrites, which result both from integrating synaptic inputs and back-propagating action potentials (bAPs) from the soma, contribute to plasticity. Mapping these dynamics in the dendritic arbors of live animals is crucial for understanding neuronal computation and plasticity rules. Here we combine targeted channelrhodopsin activation with dual-plane structured illumination voltage imaging for simultaneous monitoring of dendritic and somatic voltage response dynamics in cortical layer 2/3 pyramidal neurons in anesthetized and awake mice. We examined the integration of synaptic inputs and compared the dynamics of optogenetically evoked, spontaneous and sensory-evoked subthreshold and bAP dynamics. Our measurements revealed a broadly correlated membrane voltage throughout the dendritic arbor and only weak signatures of electrical compartmentalization within individual dendritic branches. However, we observed strong spiking-history-dependent modulation of bAP propagation into distal dendrites. We propose that this dendritic filtering of bAPs may have a critical role in the regulation of bursting and in activity-dependent plasticity.

Neuronal information processing is governed by a complex interplay among diverse voltage-dependent ion channels distributed throughout the dendritic tree, soma and axon[1–4]. Dendrites perform two qualitatively distinct information processing tasks: they integrate synaptic inputs to determine spike times and they integrate spikes and synaptic inputs to mediate synaptic plasticity[5]. Broadly, these processes involve information flow in opposite directions: from synapse to soma and from soma to synapse. Yet, both processes interact with the same set of highly nonlinear dendritic ion channels; therefore, they must follow the same local excitation rules. A fundamental question in neurobiology is how the same set of dendritic channels mediates these two distinct tasks.

Experiments in acute brain slices have characterized many of the dendritic ion channels and their associated bioelectrical excitations[6]. While slice preparations provide valuable insights, they cannot reveal the dynamics of information processing in a living organism, where the electrotonic status of dendrites and their ion channels may be substantially different from slices, and where the spatial and temporal input patterns and modulatory tone are, in general, unknown and dependent on brain state. Previous in vivo investigations of dendritic physiology have primarily used calcium imaging[7–10], patch-clamp[11–17] or voltage imaging[18] techniques on single compartments. It has not yet been possible to record voltage in multiple dendrites and soma in vivo at the same time, a necessary step toward mapping subcellular information flow (for a review, see ref. 19).

In this study, we combined dual-plane voltage imaging with targeted optogenetic stimulation to simultaneously monitor dendritic and somatic voltage dynamics in vivo. We found that subthreshold and suprathreshold voltage signals were highly correlated across the apical dendritic arbor, with only weak evidence for electrical compartmentalization between branches. In contrast, back-propagating action potentials (bAPs) showed strong spike-history-dependent modulation of their amplitude in distal dendrites, with propagation enhanced

[1]Department of Chemistry and Chemical Biology, Harvard University, Cambridge, MA, USA. [2]Janelia Research Campus, Howard Hughes Medical Institute, Ashburn, VA, USA. [3]Department of Brain Sciences, DGIST, Daegu, Republic of Korea. [4]Department of Physics, Harvard University, Cambridge, MA, USA. [5]These authors contributed equally: J. David Wong-Campos, Pojeong Park, Byung Hun Lee. e-mail: cohen@chemistry.harvard.edu

https://doi.org/10.1038/s41593-026-02339-4

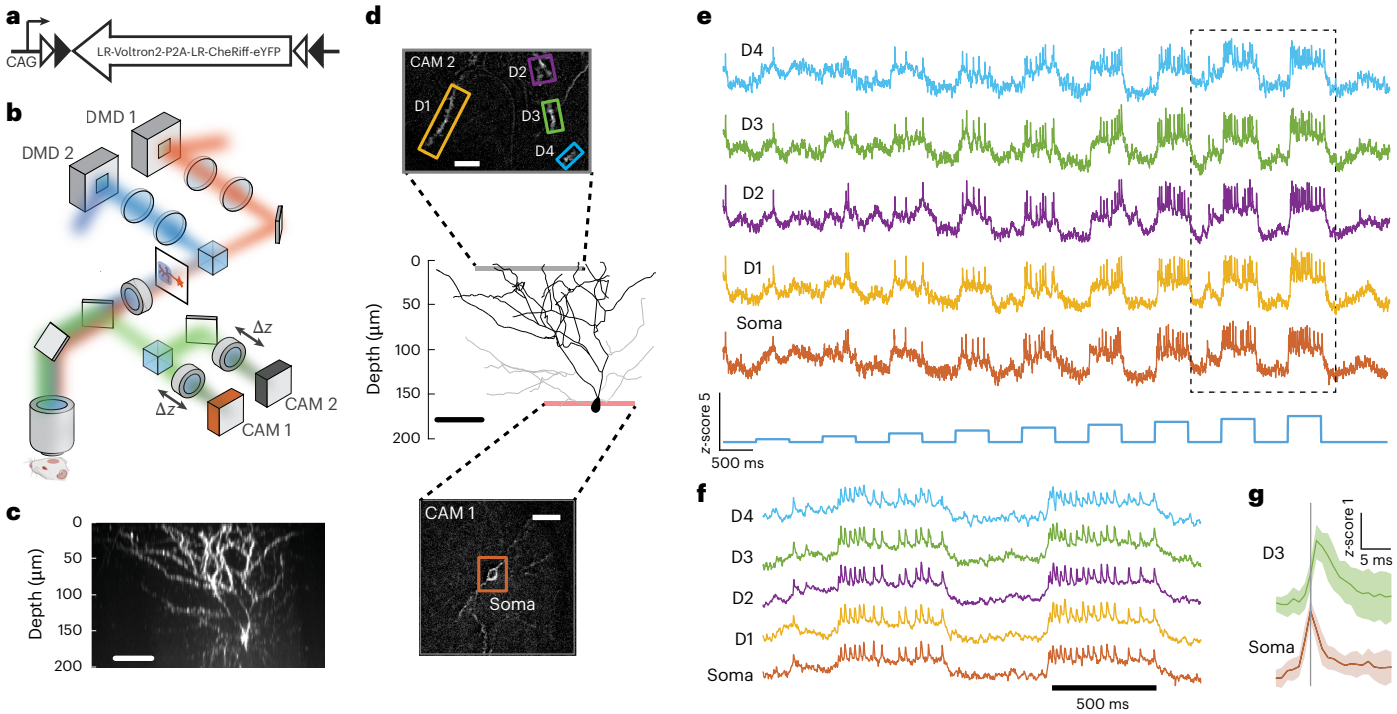

Fig. 1 | Dendritic voltage mapping and optogenetic stimulation in vivo. **a**, Construct for expressing Optopatch-V in cortical neurons, consisting of a chemogenetic voltage indicator, Voltron2, and a blue-shifted channelrhodopsin, CheRiff. The white and black triangles depict the *lox*2272 and *loxP* recombination sites, respectively. Lucy-Rho (LR) is a dendritic trafficking motif[22] and P2A is the porcine teschovirus-1 self-cleaving peptide. **b**, Instrument for targeted channelrhodopsin stimulation and structured illumination voltage imaging in two focal planes simultaneously. **c**, Side projection of a layer 2/3 pyramidal neuron from a 1-photon HiLo *z*-stack (Methods). **d**, Reconstructed morphology of the neuron in **c** and optical sections showing recording sites at the soma and at four apical dendrites. **e**, Optogenetic stimulation of the soma with pulses of increasing blue-light-intensity-evoked action potentials with increasing spike rates and corresponding bAPs in the dendrites. **f**, Close-up of the boxed region in **e** showing correspondence between somatic and dendritic events. **g**, STA of fluorescence at the soma and dendrite 3 triggered off the spike times at the soma. The dendritic events peaked after the somatic spike (solid line), as expected for back-propagation. The solid line represents the mean; the shaded regions represent the s.d. Recordings were taken at 500 Hz. Scale bars, 50 μm (**c**), 30 μm (**d**).

during accelerating spike sequences and diminished during sustained high-frequency spike trains. These results indicate that apical dendrites of layer 2/3 pyramidal cells operate as a largely unified electrical compartment while dynamically regulating bAP invasion in a manner that may shape bursting and activity-dependent plasticity.

Results

We explored the voltage dynamics of dendritic arbors in vivo by combining a chemogenetic voltage indicator, Voltron2[20], with a blue-shifted channelrhodopsin (CheRiff)[21] linked to an enhanced yellow fluorescent protein (eYFP) for visualization. We appended a Lucy-Rho[22] sequence to both the Voltron2 and CheRiff for improved membrane trafficking (Fig. 1a). We call this Voltron-based construct for all-optical electrophysiology Optopatch-V. We expressed Optopatch-V very sparsely in layer 2/3 cortical neurons in the barrel cortex of wild-type adult mice, either via in utero electroporation of a Cre-dependent construct along with dilute CAG-Cre, or via targeted single-cell electroporation (Methods). We loaded the Voltron2 with a bioavailable HaloTag ligand dye, JF608, to enable red light voltage imaging (Methods).

The home-built imaging system contained two digital micromirror devices (DMDs) for independent dynamic targeting of blue light (488 nm, for optogenetic stimulation) and orange light (594 nm, for structured illumination voltage imaging). The optical system (Supplementary Figs. 1 and 2) and custom cranial window adapter (Supplementary Fig. 3) were designed to minimize optical aberrations (Methods). We patterned the orange illumination to selectively illuminate the imaged subcellular structures (dendrites or soma), thereby achieving confocal-like optical sectioning and minimizing fluorescence from out-of-focus objects. The orange light propagated well in brain tissue, permitting structural imaging to depths of 200–300 μm (Supplementary Fig. 4). In the imaging path, we acquired simultaneous recordings from the soma and apical dendrites by splitting the fluorescence between two cameras whose focal planes could be adjusted independently (Fig. 1b). Custom instrument-control software ensured microsecond-precision synchrony and subpixel spatial registration between both cameras and both DMDs (Methods).

Our measurement protocol consisted of several steps to ensure faithful recordings of dendritic voltage signals. We used a fluorescent blood tracer to map the capillaries and avoid imaging dendrites close to capillaries (Supplementary Fig. 5). Before each functional recording, we acquired a high-resolution *z*-stack around each dendritic branch, which we used to quantify and correct subsequent z-motion during the functional recording (Supplementary Fig. 6). We also acquired whole-cell structural maps to ensure that all recorded dendrites belonged to the same target neuron (Methods). By comparing the amplitude of fluorescence fluctuations at the in-focus images of the dendrites to fluctuations in interstitial regions between dendrites, we determined that the combined contribution of out-of-focus and scattered fluorescence to the dendritic fluorescence signals was 9.0 ± 6.2% (mean ± s.d., $n = 14$ branches, ten cells; Supplementary Fig. 6), a consequence of the structured excitation. This measurement placed an upper bound on the spurious correlations between dendritic branches because of shared out-of-focus sources. We further confirmed the absence of branch-to-branch optical crosstalk in cases where labeled branches from neighboring neurons appeared in the same field of view ($n = 3$ neuron pairs). In these cases, the signals from the two branches showed

distinct spiking and subthreshold dynamics (Supplementary Fig. 7). Postprocessing analysis corrected for in-plane and axial motion, blood flow and photobleaching and extracted fluorescence signals whose spatial footprint corresponded to the in-focus dendrite images (Methods and Supplementary Fig. 8).

We performed simultaneous patch clamp recordings and voltage imaging in acute brain slices to characterize the fidelity of the voltage recordings (Supplementary Fig. 9). Spikes were detected optically with 100% fidelity and zero false positives, at up to the maximum observed spike rate of ~100 Hz (>2,000 spikes). Spikes recorded by patch clamp had a full width at half-maximum (FWHM) of 1.14 ± 0.04 ms (mean ± s.d.; n = 127 spikes), but downsampling the electrical trace to 1 kHz gave an apparent FWHM of 1.7 ± 0.2 ms. The single-trial optical recordings at 1 kHz had an FWHM of 2.3 ± 0.3 ms, primarily broadened by the 0.7-ms response time of the voltage indicator. For a detailed characterization of the fidelity, temporal resolution and spatial resolution of the voltage imaging, see ref. 23. For experiments that focused on spike detection or subthreshold dynamics, we acquired movies at 500 Hz; for experiments concerning spike timing, we acquired at 1 kHz (Methods).

By combining a red-shifted voltage indicator, very sparse expression and structured illumination HiLo microscopy[24], we could map and record neuronal compartments to a depth of 230 µm in vivo (Methods, Supplementary Fig. 10 and Supplementary Video 1). Figure 1c shows a side view of a HiLo z-stack of a single neuron; Fig. 1d shows a skeletonized view of the same cell, with one somatic and four apical dendrite recording sites. We stimulated the neuron with 0.5-s pulses of blue light across the entire neuron at increasing intensity and simultaneously recorded from the soma and four dendrites (Fig. 1d,e). We observed robust blue-light-evoked spiking in the soma and bAPs in the dendrites (Fig. 1f). Spike-triggered average (STA) bAP waveforms confirmed that the soma spiked first and that the spike waveform was broader in the dendrites than in the soma, as expected for bAPs (Fig. 1g).

Mapping bAP propagation

We mapped the propagation of bAPs by keeping one camera (CAM 1) focused on the soma and moving the field of view and focus of the second camera (CAM 2) across different branches of the dendritic arbor. These experiments were performed in anesthetized mice to maximize the long-term stability of these multi-site recordings. Distances from the soma to the recording sites and between recordings sites were determined from the contour distances along the three-dimensional reconstruction of the dendritic trees (Supplementary Fig. 11).

For each CAM 2 field of view, we evoked a spike train via blue light pulses targeted to the soma (40 pulses, 8-ms duration, 5 Hz) and recorded the spikes at the soma and the bAPs in the dendrites (Fig. 2a–c). To verify that bAP propagation was not influenced by out-of-focus CheRiff activation in the dendrites, we repeated the measurements using a soma-targeted CheRiff construct (Methods). The bAP propagation speed and attenuation were similar for the soma- targeted and broadly trafficked CheRiff (Supplementary Fig. 12) so data from both constructs were pooled (32 dendrites, six neurons, six mice for widely trafficked CheRiff; 37 dendrites, six neurons, six mice for soma-targeted CheRiff).

We used a background-robust estimate of $\Delta F/F$ to ensure that signals were proportional to local voltage (Methods and Supplementary Fig. 13) and then calculated the mean bAP waveforms at each recording site (Fig. 2d), triggered by the peak timing at the soma. We quantified local bAP amplitude by the peak $\Delta F/F$ during the event, measured relative to a baseline determined during a non-spiking epoch 10–40 ms before the event (Methods). We combined multiple recordings from different dendritic locations within each single cell to create comprehensive three-dimensional maps of bAP propagation (Fig. 2e and Supplementary Video 2). The mean bAP peak amplitude decayed as a function of contour distance from the soma, with an exponential length constant of 211 ± 18 µm (95% confidence interval (CI), n = 69 dendrites, 12 neurons, 12 mice; Fig. 2f).

Back-propagation delays of the peak depolarization increased nonlinearly with contour distance from the soma, from ~1.5 ms at 50 µm to 4 ms at 280 µm (Fig. 2g), similar to prior patch clamp results in acute brain slices[25]. The bAP conduction speed within the first 200 µm was 0.217 ± 0.05 ms (95% CI, n = 69 dendrites, 12 neurons, 12 mice), similar to prior results in brain slices[23,25]. The slower conduction at a larger distance is probably due to cable filtering in the increasingly narrow distal branches. These experiments demonstrated that temporally isolated single-action potentials back-propagated efficiently throughout the apical tree of layer 2/3 pyramidal cells, with distal sites receiving bAP-mediated depolarization at increased time delay and decreased amplitude compared to perisomatic ones.

We next analyzed the trial-to-trial variability in the bAP propagation. Across all dendritic recording sites, bAP amplitude in the dendrite and soma had a mean correlation of R = 0.51 ± 0.15 (95% CI, n = 994 bAPs, 69 dendrites, 12 neurons, 12 mice) with a decrease to R = 0.24 ± 0.17 at soma–dendrite distances greater than 200 µm ($P < 10^{-15}$, Wilcoxon rank-sum test; Fig. 2h,i). The bAP amplitude was also correlated between simultaneously recorded dendritic branches, with a mean correlation of R = 0.60 ± 0.14 (95% CI, n = 973 bAPs, 38 dendrite pairs, nine neurons, nine mice; Fig. 2j,k). The smaller number of neurons in this analysis is because some neurons did not have pairs of simultaneously recorded dendrites. The correlation in bAP amplitude between branches did not decrease detectably with increasing branch-to-branch contour separation, up to the maximum measured separation of 460 µm. We did not observe branch-specific bAP failures. Together, these results imply that under these conditions, the apical dendritic tree behaved primarily as a single electrical compartment, that is, distal apical dendrites had larger fluctuations in bAP amplitude relative to the soma than relative to each other.

Correlated dynamics between dendrites

We next probed the electrical coupling between dendritic branches. Some models of dendritic computation have proposed that dendrites act as distinct computational units[26,27]. For this to be true, one would expect to observe different voltage dynamics between the dendrites of a given cell. We recorded the spontaneous activity in groups of 3–5 dendrites simultaneously, with contour-length separations of 70–335 µm. In both anesthetized and quietly awake mice, we observed subthreshold fluctuations similar to previously reported up-states and down-states[28,29]. State transitions occurred synchronously across dendrites; the fine-scale dynamics also appeared highly correlated between the dendritic branches (Fig. 3a–c).

To quantify these observations, we calculated pairwise cross-correlations of the spontaneous subthreshold dynamics versus contour distance (Methods and Supplementary Fig. 14a). The correlation depended on brain state and decreased gradually with contour distance, with length constants 1,300 ± 250 µm for anesthetized and 540 ± 66 µm for awake mice (95% CI, n = 61 dendrite pairs, seven neurons, seven mice; Fig. 3d). For pairs separated by more than 300 µm, dendrites displayed a subthreshold cross-correlation R = 0.73 ± 0.14 (95% CI) in the anesthetized state and R = 0.50 ± 0.17 in the awake state. Upon accounting for the effect of photon-shot-noise on degrading the cross-correlations (Methods and Supplementary Fig. 15), the upper bounds on the dendrite–dendrite cross-correlations (assuming identical underlying voltage dynamics) were estimated to be 0.94 ± 0.02 (anesthetized) and 0.85 ± 0.04 (awake). These results imply that the spontaneous subthreshold electrical dynamics were largely shared throughout the dendritic tree in layer 2/3 apical dendrites in both anesthetized and quietly awake states (although less strongly shared in awake mice).

We searched for deviations from these highly correlated dendritic dynamics during minute-long recordings in the awake and anesthetized

https://doi.org/10.1038/s41593-026-02339-4

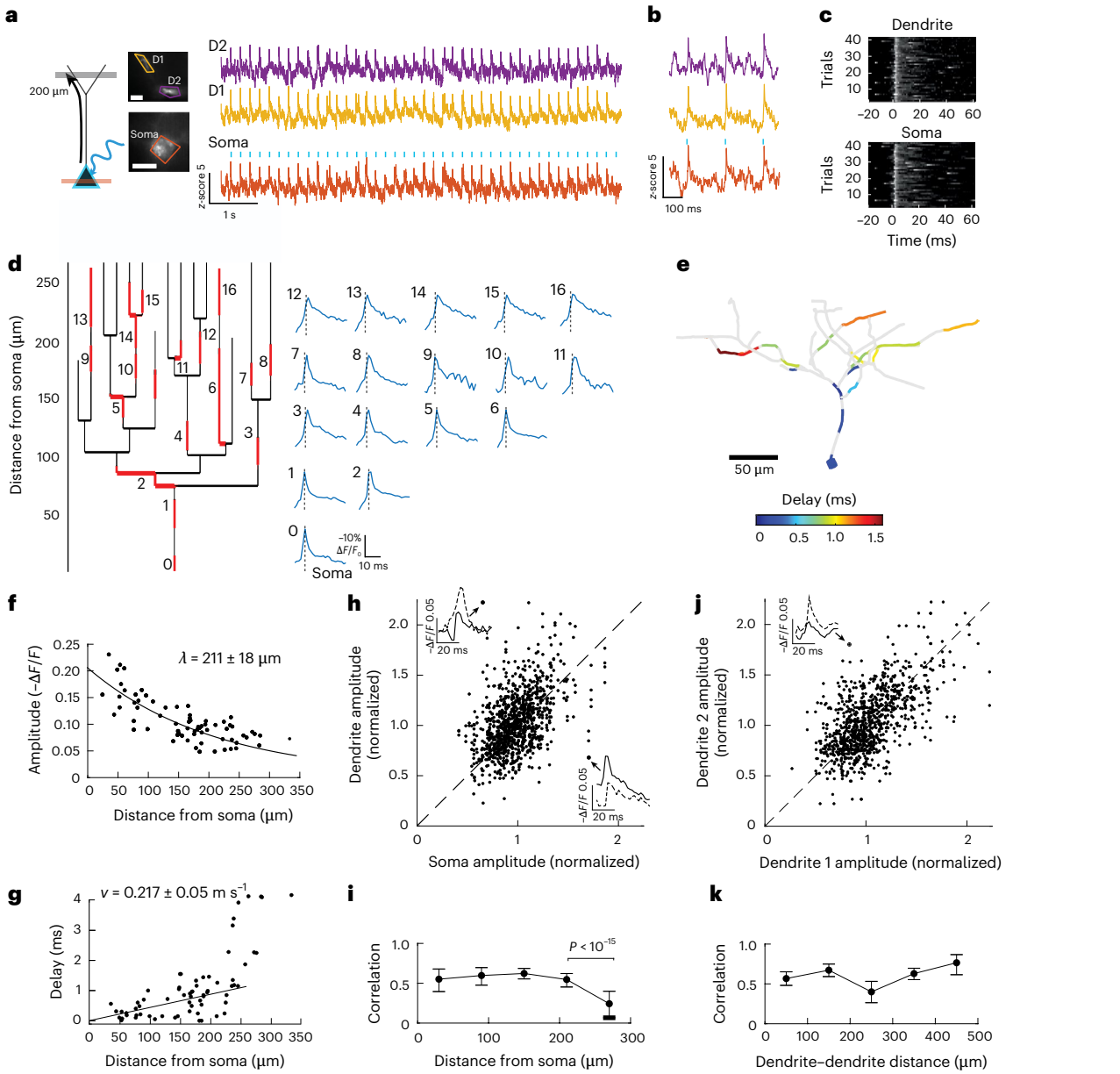

Fig. 2 | Mapping back-propagating action potentials in vivo. a, Protocol for measuring bAP delays. Optogenetic stimuli were targeted to the soma to evoke spikes; the mean fluorescence responses in the dendrites were calculated, triggered off the soma spike times. Combining many such measurements, always referenced to the soma spike times, yielded a map of bAP delays. **b**, Representative single-trial recordings at the soma and two dendrites. **c**, Stimulus-aligned raster showing fluorescence dynamics for 40 evoked spikes within a single recording. **d**, Left: dendrogram depicting 16 dendritic recording sites (red). Right: STAs triggered off the soma spikes. The vertical dashed lines indicate the timing of spike peak at the soma. $\Delta F/F$ and the time scalebar apply for all recording sites. **e**, Three-dimensional reconstruction of bAP delays in apical dendrites. See also Supplementary Video 2. **f**, Mean amplitude ($-\Delta F/F$) of bAPs versus contour distance from the soma. **g**, Mean peak delay versus contour distance from the soma. **h**, Scatterplot of the bAP amplitudes recorded at the soma and dendrites. The bAP amplitude at each recording site was normalized to its mean. Average correlation 0.51 ± 0.15 (95% CI, n = 994 bAPs). Top left inset: Example of a high dendritic amplitude (dashed) and low somatic amplitude (solid). Bottom right inset: Example of a low dendritic amplitude (dashed) and high somatic amplitude (solid). **i**, Soma–dendrite correlation in bAP amplitude as a function of soma–dendrite contour distance. For distances greater than 200 µm, soma–dendrite correlations were significantly lower ($P < 10^{-15}$, two-sided Wilcoxon rank-sum test). For **f**–**i**, n = 70 dendrites, 12 neurons and 12 mice. **j**, Scatterplot of the bAP amplitudes recorded simultaneously in pairs of dendrites. bAP amplitude at each recording site was normalized to its mean. Average correlation 0.60 ± 0.14 (95% CI, n = 973 bAPs). Inset: an example of an event with different amplitudes between two dendrites. **k**, Dendrite–dendrite correlation in bAP amplitude as a function of dendrite–dendrite contour distance. For **i** and **k**, data are presented as mean values ± 95% CIs calculated using bootstrap resampling. For **j** and **k**, n = 38 dendrite pairs, 9 neurons and 9 mice. Recordings were taken at 1 kHz. Scale bar, 10 µm (**a**).

states (Fig. 3e). We occasionally observed isolated brief (<5 ms) events in individual dendritic branches, which did not have an accompanying spike at the soma or in other branches (Fig. 3f, Methods and Supplementary Fig. 16). We provisionally associated these to local sodium spikes. These events had a mean frequency of 0.67 per minute in anesthetized mice and 3.25 per minute in awake mice (n = 9 neurons, nine mice, paired anesthetized and awake measurements). We never observed somatic spikes triggered by these local events, that is, cases where the dendritic depolarization peaked before a somatic spike. Thus, these local events did not appear to have a role in action potential generation.

https://doi.org/10.1038/s41593-026-02339-4

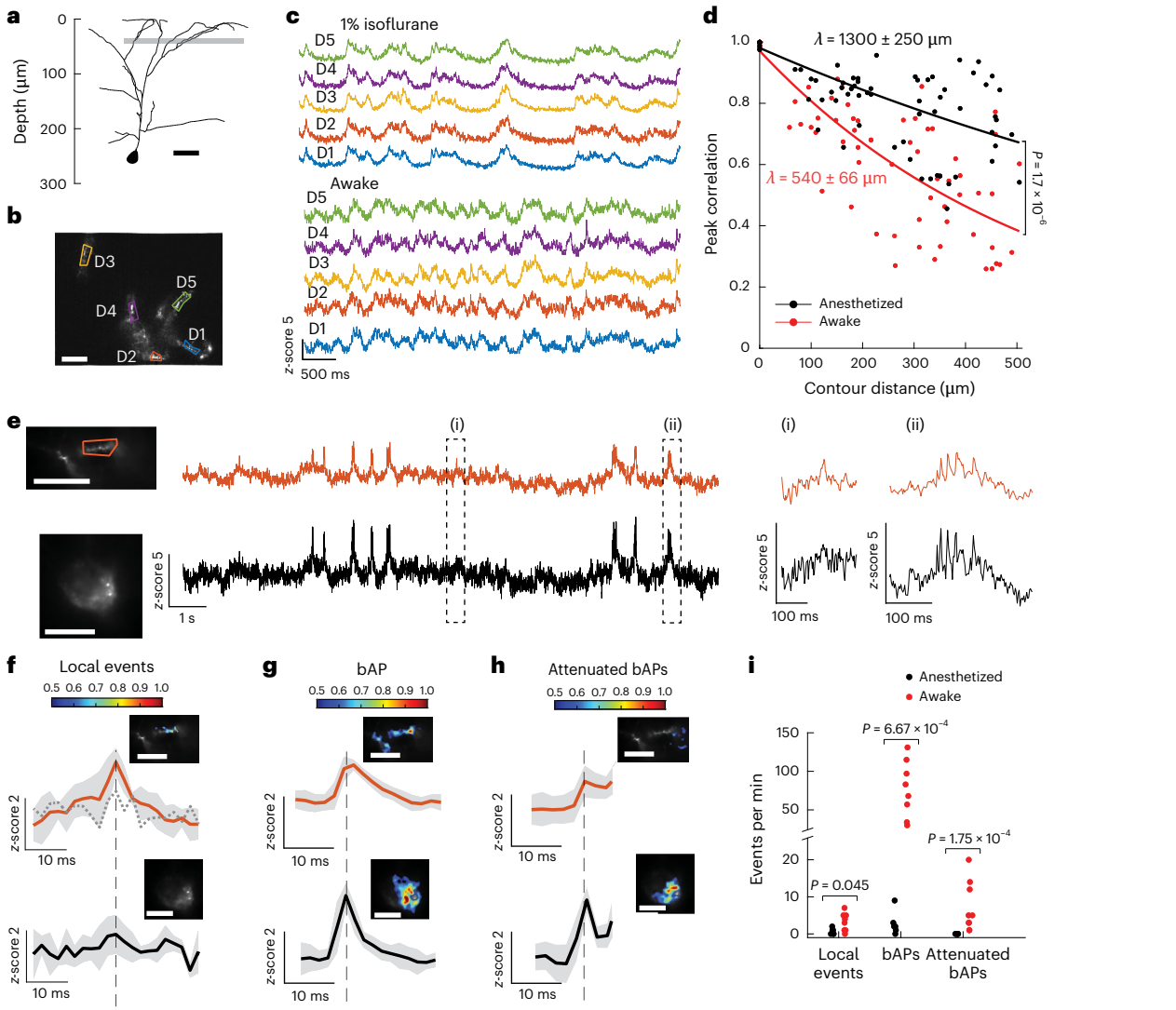

Fig. 3 | Dendritic structure of spontaneous dynamics. a, Representative neuron with concurrent recordings from five dendritic branches. **b**, Mean fluorescence of Voltron2 in the recorded dendritic branches. **c**, Recordings of spontaneous activity at (top) 1% isoflurane and (bottom) in the awake state. **d**, Pairwise cross-correlation versus contour distance between recorded branches. Correlations decayed with an exponential length constant of 1,300 ± 250 µm (anesthetized) and 540 ± 66 µm (awake; mean ± s.d., $n = 61$ dendrite pairs, 7 neurons and 7 mice). For contour distances greater than 300 µm, the pairwise correlations in the awake state were significantly lower than in the anesthetized state ($P = 1.7 \times 10^{-6}$, two-sided Wilcoxon signed-rank test). **e**, Spontaneous activity in the awake state showing (i) local dendritic events and (ii) bAPs. **f**, Event-triggered averages of local dendritic excitations ($n = 4$ events). **g**,**h**, bAPs ($n = 74$ events) (**g**) and attenuated bAPs ($n = 5$ events) (**h**), all recorded in the same neuron and dendrite. The first bAP in a burst was attenuated relative to the others; these were defined as 'attenuated bAPs'. Insets: the spatial footprints of the events. The color bars show the event amplitude relative to the local dendritic event for **f** and the somatic spike for **g** and **h**. The solid line represents the mean, with the shaded regions as the s.d. **i**, Mean frequencies of the different types of neuronal excitations ($n = 9$ neurons, 9 mice; each point represents a neuron). $P = 0.045$ for local events, $P = 6.67 \times 10^{-4}$ for bAPs, $P = 1.75 \times 10^{-4}$ for attenuated bAPs. All event frequencies were compared using a two-sided Wilcoxon rank-sum test. Recordings were taken at 500 Hz. Scale bars, 20 µm (**b**,**e**–**h** for dendrites), 10 µm (**e**–**h** for somas).

Optogenetic stimuli targeted to individual dendritic branches typically produced subthreshold responses primarily localized to the targeted branch (four neurons, four mice; example shown in Supplementary Fig. 14) or, under stronger stimulation, bAPs which originated near the soma (Methods and Supplementary Fig. 17). Targeted photo-stimulation occasionally evoked localized brief (<5 ms) dendritic excitations, which did not evoke spikes at the soma (Supplementary Fig. 17). Thus, our approach can detect localized dendritic depolarizations and excitations in vivo, although such events were rare in our data.

In paired somatic and dendritic recordings, we observed spontaneous bAPs in both the anesthetized (2.8 per min) and awake (77 per min) states (Fig. 3g, 28 dendrites, 9 neurons, 9 mice). During spike bursts, the first bAP amplitude across the sampled dendritic compartments was simultaneously attenuated relative to subsequent bAPs in the same burst and at the same locations. These attenuated bAPs occurred in both the awake state (7.4 per min; Fig. 3h) and very rarely during anesthesia (<1 per min). We did not observe branch-specific bAP failures or attenuation, which is consistent with our prior observations that optogenetically evoked bAP amplitudes largely covaried across branches. All three classes of events occurred more frequently in the awake state than under anesthesia (Fig. 3i; $p = 0.045$ for local events, $p = 6.67 \times 10^{-4}$ for bAPs, $p = 1.75 \times 10^{-4}$ for attenuated bAPs; two-sided Wilcoxon rank sum test).

The strong correlations of spontaneous subthreshold voltages across dendrites, together with the shared variations of spontaneous

https://doi.org/10.1038/s41593-026-02339-4

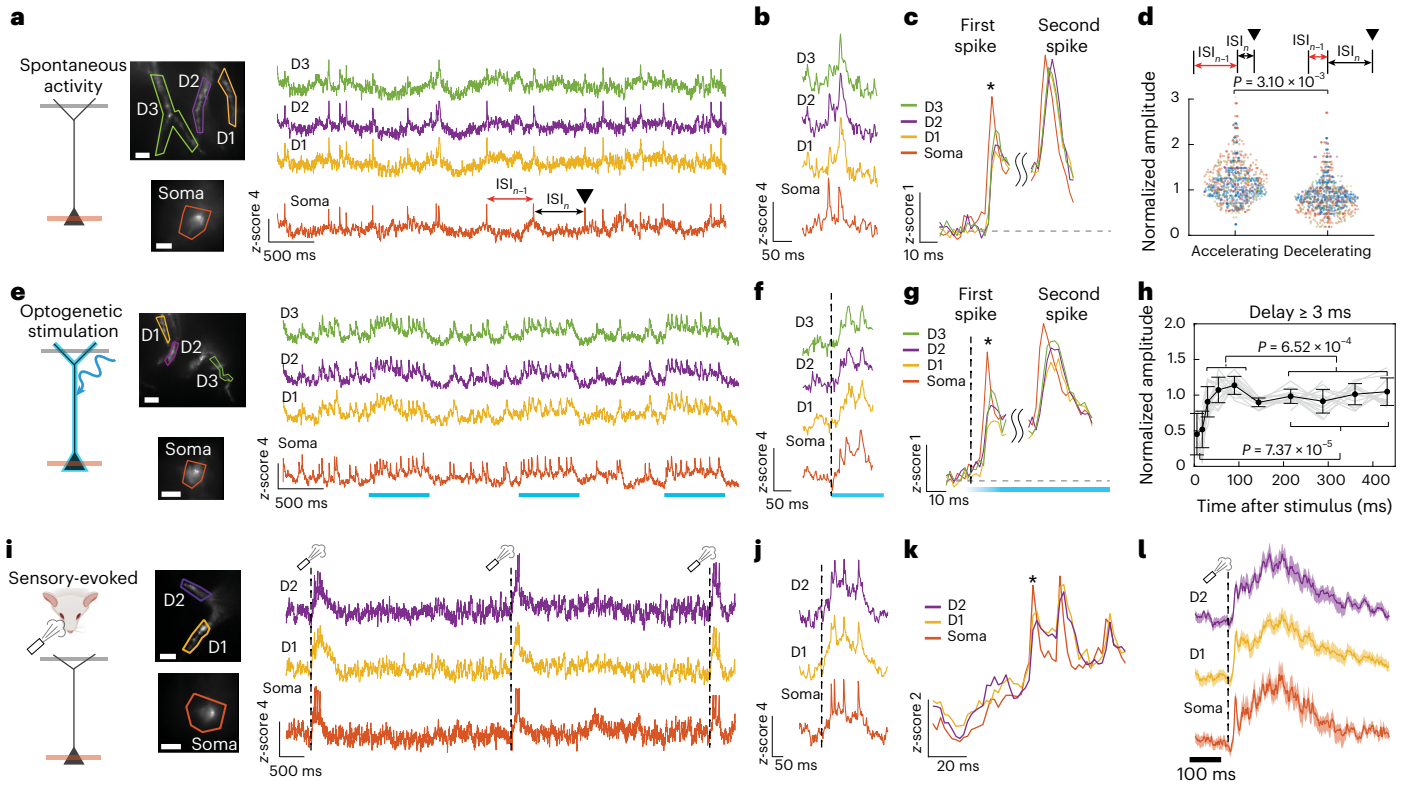

Fig. 4 | History-dependent back-propagation in bursts. a, Spontaneous activity. Spike timing was characterized by the ISI one step (ISI_n) and two steps (ISI_{n-1}) before a reference spike (black triangle). **b**, Single-trial recording of a spike doublet where the first bAP was attenuated relative to the second in the distal dendrites. **c**, STA waveform showing attenuation of the first bAP (asterisk) relative to the second. Events were triggered off the respective spike peaks at the soma (doublet ISIs 18 ± 7 ms). **d**, Comparison of bAP propagation for accelerating and decelerating spontaneous spike rates. The colors correspond to different cells. Accelerating: $ISI_{n-1} > 75$ ms, $ISI_n < 75$ ms; decelerating: $ISI_{n-1} < 75$ ms, $ISI_n > 75$ ms ($n = 238$ spike triplets, 20 branches, 5 neurons and 5 mice). Amplitudes are normalized relative to the mean second spike amplitude across triplets of a given class (accelerating or decelerating). A two-sided Wilcoxon signed-rank test gives $P = 3.10 \times 10^{-3}$ for each group, when compared to 1. **e**, Sustained (400-ms) blue light pulses targeted to the soma evoked tonic firing at the soma and corresponding bAPs at the dendrites. **f**, Single-trial recording of an optogenetically evoked spike train where the first bAP was attenuated in the distal dendrite relative to subsequent bAPs in the same burst. **g**, STA waveform showing attenuation of the first bAP (asterisk) relative to subsequent bAPs, triggered off the corresponding spikes in the soma (asterisk, $n = 10$ trials, from neuron in **e**). **h**, Biphasic dynamics of bAP amplitude in distal dendrites as a function of time after stimulus onset. Initial bAPs were attenuated, followed by a window of enhanced bAP amplitude, and then a decrease ($n = 21$ dendrites, 7 neurons and 7 mice). Data are presented as the mean ± s.d. $P = 7.37 \times 10^{-5}$ at onset, $P = 6.52 \times 10^{-4}$ for 50–100 ms after stimulus versus steady state; two-sided Wilcoxon rank-sum test. **i**, Air puff sensory stimulation evoked bursts of spikes in the soma and bAPs in the dendrites. **j**, Single-trial recording of a sensory-evoked burst where the first bAP was attenuated relative to subsequent bAPs. **k**, STA waveform showing attenuation of the first bAP relative to subsequent bAPs in distal dendrites ($n = 13$ trials). Events were triggered off the first spike peak at the soma. **l**, Stimulus-triggered average responses showing a fast depolarization followed by a sustained plateau potential. Line and shading: mean ± s.d. Recordings were taken at 500 Hz. Scale bars, 10 µm (**a**,**e**,**i**).

bAP amplitudes, could be explained by (1) strong electrotonic coupling between dendrites and/or (2) correlated inputs to distinct dendritic branches. Targeted photo-stimulation primarily evoked localized depolarizations, despite possible off-target stimulation of neighboring branches from scattered or out-of-focus blue light (Supplementary Fig. 14f); while spontaneous dynamics were highly correlated between branches in concurrent measurements on the same cell (Supplementary Fig. 14c). This observation indicates that spontaneous correlations primarily reflect correlated inputs, rather than direct biophysical voltage coupling. Indeed, a previous report on paired patch clamp recordings on neighboring pyramidal cells in lightly anesthetized rat somatosensory cortex revealed highly correlated ($R \approx 0.75$) subthreshold voltages, indicating a largely shared synaptic input field across nearby cells[30]. It is thus not surprising that neighboring branches of a given cell would receive correlated synaptic inputs.

Accelerating spike rate favors spontaneous bAP propagation

As the most pronounced signature of dendritic nonlinearities appeared to be global spike-to-spike variation of bAP amplitude in distal dendrites, we next explored history-dependent properties of bAPs. To study how dendrites mediate bAP propagation, we recorded spontaneous activity at the soma and apical dendrites in awake mice. In some cells, we observed spike doublets with a narrow distribution of inter-spike intervals ((ISIs), 18 ± 7 ms, mean ± s.d., $n = 238$ spike triplets, 20 branches, 5 neurons, 5 mice; Fig. 4a). Examination of individual spike doublets (Fig. 4b and Supplementary Fig. 18) as well as the average doublet waveforms (Fig. 4c) revealed that in the distal dendrites the first bAP was largely attenuated relative to the second bAP.

To quantify this effect, we classified changes in spike rate in trios of consecutive spikes by the ISI one step (ISI_n) and two steps (ISI_{n-1}) before a reference spike (arrow in Fig. 4a). We defined accelerating trios as $ISI_{n-1} > 75$ ms and $ISI_n < 75$ ms and vice versa for decelerating (Fig. 4d). In distal dendrites, the third bAP in accelerating trios experienced amplification relative to the second bAP, while the third bAP in decelerating trios experienced suppression relative to the second. Thus, spontaneous bAP propagation in vivo is influenced by the rate of change of firing, favoring an accelerating spike rate. This finding is consistent with prior numerical simulations showing that bursting in cortical neurons (indicative of bAP-triggered dendritic excitations) is favored by a rising input slope[31].

Optogenetically triggered accelerating spike rate favors bAP propagation

As spontaneous spikes are evoked by synaptic inputs, the observations above could reflect either intrinsic properties of dendritic excitability or an aspect of the synaptic inputs around the time of the spike doublet (for example, changes in shunting from balanced excitation and inhibition). To resolve this ambiguity and to gain independent control of the spike timing, we stimulated the cells with sustained (>400-ms) pulses of blue light while recording from the soma and dendrites (Fig. 4e). These pulses produced sustained firing at the soma and corresponding bAPs in the dendrites. As the timing of the optogenetic stimuli was uncorrelated with the spontaneous synaptic dynamics, the stimulus-triggered average bAP propagation reflected the intrinsic excitability properties of the dendritic tree.

We calculated the average bAP amplitudes in distal dendrites (bAP peak delay greater than 3 ms relative to peak at soma) as a function of time after stimulus onset. As in the spontaneous activity, the first bAP in each spike train was highly attenuated in the dendrites relative to later bAPs measured at the same locations (50 ± 26% versus bAPs 200–450 ms after stimulus onset, mean ± s.d., $P = 7.37 \times 10^{-5}$, two-sided Wilcoxon rank-sum test; $n = 21$ dendrites, seven cells, seven mice; Fig. 4f–h). From 50–100 ms after stimulus onset, bAP amplitude increased above the steady state (113 ± 12% versus bAPs 200–450 ms after stimulus onset, mean ± s.d., $P = = 6.52 \times 10^{-4}$, two-sided Wilcoxon rank-sum test). To test whether spurious out-of-focus channelrhodopsin stimulation affected these results, we repeated the experiments with soma-targeted CheRiff and observed similar strong attenuation of the first bAPs in a burst, relative to later bAPs (Supplementary Fig. 19). As a control, we verified that history-dependent modulations of bAP amplitude were not apparent in more proximal apical dendrites (bAP peak delay less than 3 ms, $n = 30$ dendrites, 11 neurons, 11 mice; Supplementary Fig. 20). Together, these results establish that the history-dependent modulation of bAP amplitude in distal dendrites is an intrinsic feature of dendritic excitability, independent of whether the spikes are triggered by synaptic inputs or optogenetic stimuli.

Sensory-evoked accelerating spike rate favors bAP propagation

Finally, we studied whether the propagation patterns observed for spontaneous and optogenetically evoked spikes also applied to sensory-evoked activity. Air puff stimulation (Methods) to the contralateral whiskers in awake mice evoked bursts of activity in both somas and dendrites (Fig. 4i) with all detected fast dendritic spikes (putative sodium spikes) initiating as bAPs from the soma. Examination of the single-trial responses (Fig. 4j) and the average evoked waveforms (Fig. 4k) revealed that the first spike in the burst was typically attenuated in the distal dendrites relative to later spikes ($n = 13$ trials). The average dendritic waveform showed a fast sensory-evoked upstroke, followed by a sustained plateau depolarization which lasted ~400 ms, substantially longer than the stimulus. Mean sensory-evoked depolarizations lasted (FWHM) 240 ± 99 ms for the soma and 220 ± 140 ms for the dendrite ($n = 4$ neurons, four mice). This plateau may reflect a dendritic plateau potential (for example, an *N*-Methyl-D-aspartate (NMDA) spike), although it may also have contributions from sustained synaptic input.

Discussion

Techniques to study subcellular voltage dynamics in vivo are critical for understanding neural computation and plasticity. In this study, we presented an all-optical approach to investigate dendritic signal processing, focusing on layer 2/3 pyramidal neurons in the barrel cortex of awake and anesthetized mice. We combined dual-plane voltage imaging with targeted optogenetic stimulation to study bidirectional electrical couplings between dendrites and soma, at both the subthreshold and suprathreshold level.

Overall, our findings indicate that under conditions of quiet wakefulness and anesthesia, spontaneous electrical dynamics, both subthreshold (Fig. 3c,d) and suprathreshold (Fig. 2h–k), are largely shared throughout the apical dendritic tree of layer 2/3 pyramidal cells. Under these conditions, the primary role of fast dendritic excitations (putative sodium spikes) was in history-dependent modulation of bAP propagation (Fig. 4), rather than in dendritic integration. Sensory inputs, combined with bAPs, evoked broadly distributed apical dendritic plateau potentials (putative NMDA spikes; Fig. 4i–l), which may provide the somatic drive that mediates sensory-evoked spike bursts. Whether these findings apply in other brain states, behavioral contexts or neuron types, remains to be determined.

A step-increase in spike rate induced a biphasic bAP propagation motif (relative attenuation-amplification-attenuation, Fig. 4h). This motif resembles the dynamics we previously observed in an analogous experiment in CA1 pyramidal cells in acute slices[23]. In that work, pharmacological perturbations ascribed the initial suppression of bAP propagation to a shunt by distally enriched A-type potassium channels[32]. Upon depolarization of the distal dendrites, these channels inactivated over a ~15-ms timescale, permitting subsequent bAPs to engage dendritic Na_V channels, leading to dendritic sodium spikes. Dendritic patch clamp experiments in cortical layer 5 pyramidal cells have also reported that in 80-Hz bAP doublets, the first bAP is attenuated relative to the second[33]. Upon sustained spiking, the subsequent decrease in bAP propagation is probably due to dendritic sodium channel slow inactivation[34].

There are also some differences between the present results and our previous voltage imaging experiments in CA1 pyramidal cells in acute slices. In CA1 acute slices, we observed a robust bimodal distribution of bAP amplitudes in the distal dendrites: bAPs either engaged dendritic Na_V channels and triggered a dendritic spike ('bAP successes'), or failed along the apical trunk ('bAP failures')[23]. In the present experiments, we observed a unimodal distribution of bAP amplitudes (Fig. 2h): there was not a clear boundary between bAP success and failure. We speculate that this difference may be a consequence of dynamic neuromodulatory and synaptic inputs in vivo leading to variable availability of apical ion channels, but we cannot rule out contributions from intrinsic differences between layer 2/3 versus CA1 pyramidal cells.

The biphasic bAP attenuation-amplification-attenuation motif observed previously in CA1 (ref. 23) and in this study in layer 2/3 pyramidal cells (Fig. 4h) suggests that the dendrites act as a spike rate accelerometer: neither single spikes nor sustained high-frequency spike trains reach the dendrites efficiently, but an increase in somatic spike rate opens a transient window for efficient bAP propagation and engagement of excitatory dendritic ion channels. This motif has important implications for learning rules: it suggests that bursts, not individual spikes, will be most effective at triggering dendritic Ca^{2+} and NMDA spikes, leading to dendritic calcium influx, and thereby engaging activity-dependent plasticity[35,36]. Dendritic bAP filtering also provides a means for upward-ramping synaptic inputs to trigger bursts, as predicted theoretically[31].

Dendritic patch clamp recordings in layer 2/3 pyramidal cells in the barrel cortex of urethane-anesthetized rats found that spontaneous sodium spikes were initiated at the soma, which is consistent with our findings in awake mice[16]. These experiments also reported that spiking history did not modulate bAP amplitude in the dendrites, contrary to our findings in awake mice. This difference may reflect greater cholinergic drive in the awake state, which is known to facilitate bAP propagation in a history-dependent manner[37,38]. The patch clamp recordings reported that strong (>0.5 nA) current injection into dendrites could evoke local dendritic plateau potentials accompanied by local Ca^{2+} increase. Similar current-evoked responses were seen in barrel cortex layer 5 pyramidal cells of awake mice[17]. We did not observe these

plateau potentials under optogenetic stimulation, probably because the optogenetic stimuli were weaker (typically <100 pA).

Dendritic patch clamp recordings in the visual cortex of awake and lightly anesthetized mice reported dendritic plateau potentials topped with rapid Na^+ spikes[12]. Under whisker sensory stimulation, we also observed sustained dendritic depolarizations topped with spikes (Fig. 4i,j). Somatic drive from these dendritic plateaus probably contributed to sensory-evoked bursting. In the patch clamp studies, comparisons with somatic Ca^{2+} imaging and analysis of event statistics suggested that the fast dendritic spikes were locally generated, but concurrent electrical activity in soma and dendrites was not directly recorded. In our experiments, sensory-evoked fast dendritic spikes were almost always triggered by bAPs. We only rarely observed spontaneous dendrite-initiated sodium spikes (Supplementary Fig. 17), indicating that these events are not necessary for dendritic integration under the conditions of our experiments. It is not clear whether the discrepancy reflects the different brain regions (visual cortex versus barrel cortex) or different recording modalities (patch clamp plus Ca^{2+} imaging versus voltage imaging).

Ca^{2+} imaging studies in layer 5 pyramidal cells in behaving mice also reported largely shared excitations across the apical dendritic tree[7,17], which is consistent with our findings based on voltage imaging. Nonetheless, the correlational structure may depend on brain state. Changes in the statistical structure of synaptic excitation and inhibition may modulate the degree of dendrite–dendrite and dendrite–soma voltage correlation. For example, rapid eye movement sleep was reported to induce a decoupling of the calcium dynamics in apical dendrites from the soma of layer 2/3 pyramidal cells[39], and isoflurane anesthesia was shown to decouple apical dendrites from the soma in layer 5, but not layer 2/3 pyramidal cells[40].

Finally, we emphasize that the spatial structures of dendritic Ca^{2+} and voltage may differ substantially, as we recently observed in dual Ca^{2+} and voltage measurements in brain slices[41]. Two factors contribute to this difference. First, activation of voltage-gated calcium channels is a steeply nonlinear function of voltage. Subtle branch-to-branch variations in voltage may lead to large variations in local Ca^{2+} current. Second, in dendrites, Ca^{2+} ions diffuse ~10^5-fold more slowly than voltage. The effective buffered diffusion coefficient for calcium is $D_{Ca} \approx 20\ \mu m^2\ s^{-1}$ (refs. 42,43), whereas for voltage, $D_V = \frac{\lambda^2}{\tau} \approx 2 \times 10^6\ \mu m^2\ s^{-1}$ ($\lambda \approx 200\ \mu m$ is the electrical length constant and $\tau \approx 20$ ms is the membrane time constant). During a typical 100-ms subthreshold event, dendritic Ca^{2+} ions diffuse ~2 µm, whereas voltage reaches a steady state with an exponential decay length of ~200 µm. Together, these two effects imply that individual dendritic branches may have distinct Ca^{2+} responses[44], even while the voltage is, on average, highly correlated between branches.

Critical next steps will be to combine imaging of voltage with recordings of neurotransmitters, neuromodulators, Ca^{2+} dynamics and signaling pathways in animals engaged in tasks which activate diverse brain states. A deeper understanding of electrical propagation in dendrites could help elucidate the relationship between dendritic biophysics and information processing.

Online content

Any methods, additional references, Nature Portfolio reporting summaries, source data, extended data, supplementary information, acknowledgements, peer review information; details of author contributions and competing interests; and statements of data and code availability are available at https://doi.org/10.1038/s41593-026-02339-4.

References

1. Stuart G., Spruston N. & Häusser M. *Dendrites* (Oxford Univ. Press, 2016).
2. Spruston, N. Pyramidal neurons: dendritic structure and synaptic integration. *Nat. Rev. Neurosci.* **9**, 206–221 (2008).
3. London, M. & Häusser, M. Dendritic computation. *Annu. Rev. Neurosci.* **28**, 503–532 (2005).
4. Häusser, M., Spruston, N. & Stuart, G. J. Diversity and dynamics of dendritic signaling. *Science* **290**, 739–744 (2000).
5. Magee, J. C. & Johnston, D. Plasticity of dendritic function. *Curr. Opin. Neurobiol.* **15**, 334–342 (2005).
6. Stuart, G. J. & Spruston, N. Dendritic integration: 60 years of progress. *Nat. Neurosci.* **18**, 1713–1721 (2015).
7. Beaulieu-Laroche, L., Toloza, E. H. S., Brown, N. J. & Harnett, M. T. Widespread and highly correlated somato-dendritic activity in cortical layer 5 neurons. *Neuron* **103**, 235–241 (2019).
8. Palmer, L. M. et al. NMDA spikes enhance action potential generation during sensory input. *Nat. Neurosci.* **17**, 383–390 (2014).
9. Jia, H., Rochefort, N. L., Chen, X. & Konnerth, A. Dendritic organization of sensory input to cortical neurons in vivo. *Nature* **464**, 1307–1312 (2010).
10. O'Hare, J. K. et al. Compartment-specific tuning of dendritic feature selectivity by intracellular Ca2+ release. *Science* **375**, eabm1670 (2022).
11. Gambino, F. et al. Sensory-evoked LTP driven by dendritic plateau potentials in vivo. *Nature* **515**, 116–119 (2014).
12. Smith, S. L., Smith, I. T., Branco, T. & Häusser, M. Dendritic spikes enhance stimulus selectivity in cortical neurons in vivo. *Nature* **503**, 115–120 (2013).
13. Waters, J. & Helmchen, F. Boosting of action potential backpropagation by neocortical network activity in vivo. *J. Neurosci.* **24**, 11127–11136 (2004).
14. Margrie, T. W. et al. Targeted whole-cell recordings in the mammalian brain in vivo. *Neuron* **39**, 911–918 (2003).
15. Kamondi, A., Acsády, L. & Buzsáki, G. Dendritic spikes are enhanced by cooperative network activity in the intact hippocampus. *J. Neurosci.* **18**, 3919–3928 (1998).
16. Svoboda, K., Helmchen, F., Denk, W. & Tank, D. W. Spread of dendritic excitation in layer 2/3 pyramidal neurons in rat barrel cortex in vivo. *Nat. Neurosci.* **2**, 65–73 (1999).
17. Xu, N.-l. et al. Nonlinear dendritic integration of sensory and motor input during an active sensing task. *Nature* **492**, 247–251 (2012).
18. Liao, Z. et al. Functional architecture of intracellular oscillations in hippocampal dendrites. *Nat. Commun.* **15**, 6295 (2024).
19. Fischer, L. et al. Dendritic mechanisms for in vivo neural computations and behavior. *J. Neurosci.* **42**, 8460–8467 (2022).
20. Abdelfattah, A. S. et al. Sensitivity optimization of a rhodopsin-based fluorescent voltage indicator. *Neuron* **111**, 1547–1563 (2023).
21. Hochbaum, D. R. et al. All-optical electrophysiology in mammalian neurons using engineered microbial rhodopsins. *Nat. Methods* **11**, 825–833 (2014).
22. Shepard, B. D., Natarajan, N., Protzko, R. J., Acres, O. W. & Pluznick, J. L. A cleavable N-terminal signal peptide promotes widespread olfactory receptor surface expression in HEK293T cells. *PLoS ONE* **8**, e68758 (2013).
23. Park, P. et al. Dendritic excitations govern back-propagation via a spike-rate accelerometer. *Nat. Commun.* **16**, 1333 (2025).
24. Lim, D., Chu, K. K. & Mertz, J. Wide-field fluorescence sectioning with hybrid speckle and uniform-illumination microscopy. *Opt. Lett.* **33**, 1819–1821 (2008).
25. Spruston, N., Schiller, Y., Stuart, G. & Sakmann, B. Activity-dependent action potential invasion and calcium influx into hippocampal CA1 dendrites. *Science* **268**, 297–300 (1995).
26. Goetz, L., Roth, A. & Häusser, M. Active dendrites enable strong but sparse inputs to determine orientation selectivity. *Proc. Natl Acad. Sci. USA* **118**, e2017339118 (2021).

27. Boahen, K. Dendrocentric learning for synthetic intelligence. *Nature* **612**, 43–50 (2022).
28. Petersen, C. C. H., Hahn, T. T. G., Mehta, M., Grinvald, A. & Sakmann, B. Interaction of sensory responses with spontaneous depolarization in layer 2/3 barrel cortex. *Proc. Natl Acad. Sci. USA* **100**, 13638–13643 (2003).
29. Waters, J. & Helmchen, F. Background synaptic activity is sparse in neocortex. *J. Neurosci.* **26**, 8267–8277 (2006).
30. Okun, M. & Lampl, I. Instantaneous correlation of excitation and inhibition during ongoing and sensory-evoked activities. *Nat. Neurosci.* **11**, 535–537 (2008).
31. Kepecs, A., Wang, X.-J. & Lisman, J. Bursting neurons signal input slope. *J. Neurosci.* **22**, 9053–9062 (2002).
32. Hoffman, D. A., Magee, J. C., Colbert, C. M. & Johnston, D. K^+ channel regulation of signal propagation in dendrites of hippocampal pyramidal neurons. *Nature* **387**, 869–875 (1997).
33. Williams, S. R. & Stuart, G. J. Backpropagation of physiological spike trains in neocortical pyramidal neurons: implications for temporal coding in dendrites. *J. Neurosci.* **20**, 8238–8246 (2000).
34. Jung, H.-Y., Mickus, T. & Spruston, N. Prolonged sodium channel inactivation contributes to dendritic action potential attenuation in hippocampal pyramidal neurons. *J. Neurosci.* **17**, 6639–6646 (1997).
35. Payeur, A., Guerguiev, J., Zenke, F., Richards, B. A. & Naud, R. Burst-dependent synaptic plasticity can coordinate learning in hierarchical circuits. *Nat. Neurosci.* **24**, 1010–1019 (2021).
36. Pfister, J.-P. & Gerstner, W. Triplets of spikes in a model of spike timing-dependent plasticity. *J. Neurosci.* **26**, 9673–9682 (2006).
37. Tsubokawa, H. & Ross, W. N. Muscarinic modulation of spike backpropagation in the apical dendrites of hippocampal CA1 pyramidal neurons. *J. Neurosci.* **17**, 5782–5791 (1997).
38. Müller, W. & Connor, J. A. Cholinergic input uncouples $Ca2^+$ changes from K+ conductance activation and amplifies intradendritic $Ca2^+$ changes in hippocampal neurons. *Neuron* **6**, 901–905 (1991).
39. Aime, M. et al. Paradoxical somatodendritic decoupling supports cortical plasticity during REM sleep. *Science* **376**, 724–730 (2022).
40. Suzuki, M. & Larkum, M. E. General anesthesia decouples cortical pyramidal neurons. *Cell* **180**, 666–676 (2020).
41. Landau, A. T. et al. Dendritic branch structure compartmentalizes voltage-dependent calcium influx in cortical layer 2/3 pyramidal cells. *eLife* **11**, e76993 (2022).
42. Soler-Llavina, G. J. & Sabatini, B. L. Synapse-specific plasticity and compartmentalized signaling in cerebellar stellate cells. *Nat. Neurosci.* **9**, 798–806 (2006).
43. Hayward, R. F. & Cohen, A. E. All-optical mapping of Ca^{2+} transport and homeostasis in dendrites. *Cell Calcium* **125**, 102983 (2025).
44. Varga, Z., Jia, H., Sakmann, B. & Konnerth, A. Dendritic coding of multiple sensory inputs in single cortical neurons in vivo. *Proc. Natl Acad. Sci. USA* **108**, 15420–15425 (2011).

Methods

DNA constructs

The Cre-dependent Optopatch-V construct was generated using standard molecular cloning techniques. Briefly, the vector was linearized by double digestion using restriction enzymes (New England Biolabs) and purified using the GeneJET gel extraction kit (Thermo Fisher Scientific). DNA fragments were generated using PCR amplification and then fused with the backbones using the NEBuilder HiFi DNA assembly kit (New England Biolabs). All plasmids were verified by sequencing (Plasmidsaurus). All constructs and their sequences are available from Addgene.

The plasmids used in this study included: CAG::DIO-LR-Voltron2-TS-ER2-p2a-LR-CheRiff-TS-eYFP-ER2 (plasmid no. 203229, Addgene) and CAG::DIO-LR-Voltron2-TS-ER2-p2a-CheRiff-eGFP-ST (plasmid no. 220931, Addgene).

CAG is a strong and universal synthetic promoter[45]; DIO is the Cre-recombinase-dependent DIO (double-floxed inverse open reading frame) conditional expression motif[46], LR is the dendrite-targeting signal[22], Voltron2 is a chemogenetic voltage indicator[20], CheRiff is a blue-light-gated nonselective cation channel[21], TS is the trafficking sequence from $K_{ir}2.1$[47], p2a is a self-cleaving ribosomal skip sequence[48], ER2 is the endoplasmic reticulum export signal FCYENEV[47] and ST is the $K_V2.1$ soma-targeting sequence[49].

Animals

All procedures involving animals were carried out in accordance with the National Institutes of Health Guide for the Care and Use of Laboratory Animals and were approved by the Harvard University Institutional Animal Care and Use Committee. The in utero electroporation surgery was carried out as described previously[50]. Briefly, embryonic day 15.5-timed pregnant female CD1 mice (Charles River Laboratories) were deeply anesthetized and maintained with 2% isoflurane. The animal's body temperature was maintained at 37 °C. Uterine horns were carefully exposed and periodically rinsed with warm sterile PBS. We co-expressed the Optopatch-V construct with either the broadly trafficked (plasmid no. 203229, Addgene) or soma-targeted (plasmid no. 220931, Addgene) CheRiff, along with CAG::Cre (plasmid no. 13775, Addgene) at wt:wt 500:1. We injected 1 µl at a 1–2 mg $µl^{-1}$ total DNA concentration to the left ventricle. Electrical pulses (40 V, 50-ms duration) were delivered five times at 1 Hz using a tweezers electroporation electrode (cat. no. CUY650P5; Nepa Gene). Injected embryos were placed back into the abdominal cavity and the surgical wound was sutured with PGCL25 absorbable sutures (Patterson). Mice were housed in a vivarium maintained on a 12-h light–12-h dark cycle at an ambient temperature with food and water ad libitum.

Cranial window surgery. Surgeries were conducted on 4-week-old mice of both sexes, following the protocol outlined in ref. 51. The surgical procedure began by exposing the skull, followed by a 3-mm circular craniotomy at coordinates 3.3–3.4 mm lateral and 1.6 mm caudal relative to bregma. The craniotomy was made using a biopsy punch (Miltex). The dura mater was then carefully removed while taking measures to prevent capillary bleeding. After this, a 3-mm round cover glass (cat. no. 1217N66, Thomas Scientific), pre-glued to a custom-made stainless-steel adapter (Tecan; Supplementary Fig. 3), was inserted into the opening. This setup aimed to reduce the thickness of the glass at the brain–objective interface. To prevent any relative movement between the brain and the adapter, gentle pressure was applied and the outer ring of the adapter was securely glued. All subsequent experimental procedures were carried out at least 1 week after surgery.

In vivo single-cell electroporation. We performed targeted in vivo single-cell electroporation using two-photon microscopy as described in ref. 52. Briefly, we anesthetized 4–6-week-old mice using isoflurane and performed a craniotomy surgery. We transferred the animal into a two-photon (2 P) microscope equipped with a patch clamp system. High-resistance (12–15 MΩ) patch pipettes were pulled and filled with 5–10 µl internal solution (8 mM NaCl, 130 mM $KMeSO_3$, 10 mM HEPES, 5 mM KCl, 0.5 mM EGTA, 4 mM Mg-ATP and 0.3 mM Na_3-GTP; pH was adjusted to 7.3 using KOH and osmolality was adjusted to 285–295 mOsm l^{-1} with water) including up to 200 ng $µl^{-1}$ plasmid DNA and 50 µM Alexa Fluor 594 hydrazide (cat. no. A10438, Invitrogen). The constructs were CAG::LR-Voltron2-p2a-LR-CheRiff-TS-eYFP-ER2 (plasmid no. 203228, Addgene) or CAG::LR-Voltron2-p2a-CheRiff-eGFP-ST (Kv2.1TS) (plasmid no. 230989, Addgene). Before filling, the solution was filtered using a 0.45-µm syringe filter. Saline (0.9% NaCl) was used to bathe the exposed cortical surface and to immerse the objective lens. We applied 10–15 mbar of pressure, placed the pipette above the craniotomy at the center of the 2 P microscope field of view and observed the flow of the fluorescent dye. We then increased pressure to 100 mbar and lowered the pipette until we touched the dura, confirmed both visually and by an increase in pipette resistance. We punctured the dura with a diagonal motion of the pipette and lowered the pressure to 50 mbar while approaching the cells of interest. We used 'shadow imaging' and searched for neurons at 150–200 µm depth, keeping the amount of diffused dye low enough to prevent image saturation. When the pipette was within 50–100 µm of the target cell, we lowered the pressure to 10 mbar and approached the cells of interest. We moved the pipette toward the center of the cell until the pipette resistance increased by 10–20%. To electroporate, we released the positive pressure and applied a train of voltage pulses (Axoporator 800 A; −12V for 0.5 ms, 50 Hz for 1 s). Successful electroporation was evidenced by flow of the fluorescent dye into the cell. After the pulses, we retracted the pipette at least 50 µm before reapplying 10 mbar of positive pressure. The same pipette can be used to electroporate multiple cells by repeating these steps. After the procedure, we sealed the craniotomy with a coverslip and our metal adapter (see 'Experimental protocols') and placed the animal in a heated recovery chamber until it regained consciousness for later return to its housing. Cells were imaged 7–14 days after electroporation.

Optical system

Experiments were performed on a custom-built upright fluorescence microscope (Supplementary Fig. 1). Illumination was delivered by lasers centered at 488 nm (OBIS, 60 mW, Coherent) and 594 nm (Cobolt Mambo, 100 mW). Laser light was combined using a dichroic mirror (FF506-Di03-25 × 36, IDEX) and sent through an acousto-optic tunable filter (TF525-250-6-3-GH18A, Gooch and Housego) for modulation of each wavelength. The beams from each color were then separated by another dichroic mirror (FF506-Di03-25 × 36, IDEX) and sent to two DMDs (V-7000, Vialux). This configuration allows dynamic stimulation and recording of independent areas at two wavelengths. Light from both DMDs was merged using a dichroic mirror and converged at an intermediate image plane, which served as a point for validating the optical alignment. An excitation tube lens (cat. no. LA1417-A, Thorlabs) collected light from this intermediate image plane and sent it to a ×25 water immersion objective, 1.05 numerical aperture (XLPLN25XWMP2 ×25/1, Olympus). Fluorescence was collected by the same objective and separated from excitation light via a multiband dichroic mirror (Di01-R405/488/594-25×36, three bandpasses, IDEX). The dichroic was carefully mounted to minimize mechanical stress, which could induce astigmatism in the image.

A 50–50 beamsplitter (cat. no. BSW26R, Thorlabs) split the light into two image paths, each of which was passed through an emission filter (ET645/75m, bandpass, Chroma) placed after the beamsplitter, a tube lens (cat. no. TTL200-A, Thorlabs) on an axial translation stage, and imaged onto a scientific complementary metal-oxide-semiconductor camera (ORCA-Fusion and ORCA-Flash, Hamamatsu). The cameras were synchronized using frame-trigger pulses from a data acquisition system (cat. no. NI-PCIe-6343, National Instruments) referenced to the

output clock signal of the camera. This same clocking synchronizes the experimental waveforms that control the acousto-optic tunable filters and shutters. Field-of-view registration between the DMDs and cameras was performed using an affine transformation between a calibration pattern projected on to the DMDs consisting of three points.

Overall focus was achieved by moving the sample axially relative to the objective, while offset in the focal planes was achieved by axial translation of the tube lens in front of the second camera. A kinematic mirror before the tube lens of the second camera allowed lateral offset between the fields of view of the two cameras. Our scheme allows arbitrary control of the field of view of the second camera across $400 \times 400 \times 250\ \mu m^3$ (Supplementary Fig. 21).

Experimental protocols

Acute brain slices and electrophysiology. Coronal slices (300 µm) were prepared from CD1 mice of either sex between 2 and 4 postnatal weeks. Animals were anesthetized with isoflurane and euthanized using decapitation. The brain was then removed and placed in ice-chilled slicing solution containing (in mM): 210 sucrose, 3 KCl, 26 $NaHCO_3$, 1.25 NaH_2PO_4, 5 $MgCl_2$, 10 D-glucose, 3 sodium ascorbate and 0.5 $CaCl_2$ (saturated with 95% O_2 and 5% CO_2). Acute slices were made using a Vibratome (VT1200S, Leica Biosystems) while maintained in the slicing solution. Slices were recovered at 34 °C for 10 min in the imaging solution (artificial cerebrospinal fluid (ACSF)) containing (in mM): 124 NaCl, 3 KCl, 26 $NaHCO_3$, 1.25 NaH_2PO_4, 2 $MgCl_2$, 15 D-glucose and 2 $CaCl_2$ (saturated with 95% O_2 and 5% CO_2). Slices were then incubated in ACSF containing JFX608-HaloTag ligand (0.5–1 µM) for 30 min at room temperature and moved to a fresh ACSF for another 30 min to wash out excess dye. Slices were maintained at room temperature until recordings were made.

We performed somatic whole-cell recordings using a custom upright microscope. All experiments were performed at 34 °C and continuously perfused at 2 ml min^{-1} with ACSF. Patch pipettes (2–4 MΩ) were filled with an internal solution containing (in mM): 8 NaCl, 130 $KMeSO_3$, 10 HEPES, 5 KCl, 0.5 EGTA, 4 Mg-ATP and 0.3 Na_3-GTP. The pH was adjusted to 7.3 using KOH and osmolality was adjusted to 285–295 mOsm l^{-1} with water. Signals were amplified using a Multiclamp 700B (Molecular Devices), filtered at 10 kHz with the internal Bessel filter, and digitized at 100 kHz using a PCIe-6323 (National Instruments) acquisition board. After entering the whole-cell configuration, membrane capacitance and membrane resistance were measured under voltage-clamp mode. To induce a rapid, isolated single spike, 2 nA current (2-ms duration) was injected into the soma in current-clamp mode.

Cranial window adapter. Commonly used three-layer cranial windows[51], consisting of three coverslips glued together, are outside the thickness range of typical microscope objective correction collars, leading to spherical aberration. To mitigate this source of aberration, stainless-steel adapters (Tecan) were designed to mount a single no. 1 coverslip against the brain surface. The adapter consists of a washer-like structure with a 150-µm protrusion in an inner ring, where the no. 1 coverslip is glued (Supplementary Fig. 3). Additionally, to counteract spherical aberration in dendrites, we incorporated a technique of imaging a dendrite and adjusting the focus in a scanning motion. Adjustments to the correction collar altered the relative symmetry of the image between the in-focus and out-of-focus planes typically displayed as a different blurred image. Correctly adjusted configurations display similar image shapes at both out-of-focus planes.

Animal tip-tilt. Coma aberration associated with sample tilts were compensated by adding a goniometer stage (MAGXY-60L-4-6M, Optics Focus) under the mouse platform. Coma aberration in dendrites is displayed as sideway blurring of the fluorescence signal. We adjusted the goniometer by observing the side blurring and refocusing for every tilt step. A correctly adjusted tip-tilt minimizes sideway blurring along the tilted axis.

Blood vessel identification. Neurites and somas below a blood vessel are subject to local variations in the absorption and scattering of the stimulating and fluorescent light, resulting in speckle noise[53]. Blood vessels were visualized by injecting a fluorescent tracer (FITC-CM-Dextran, cat. no. 74817, Sigma-Aldrich) and avoided in our recordings. We retro-orbitally delivered 100 µl of solution at a concentration of 50 mg ml^{-1} of the dye. Excitation at 488 nm allowed the tracking of the capillaries. Additionally, 2 P microscopy *z*-stacks could be used to localize all capillaries within a volume.

Dye injection and depth penetration. We characterized the light penetration across the wavelengths we used in our experiments. For the blue spectrum, we retro-orbitally injected the FITC-Dextran dye and recorded a 1 P *z*-stack. Capillaries deeper than 50 µm were not resolvable. For the red side of the spectrum, we retro-orbitally injected 100 µl of a red dye (Alexa Fluor 647-Dextran, cat. no. D22914, Thermo Fisher Scientific) at 50 mg ml^{-1} and recorded a 1 P *z*-stack. Imaging with red-shifted wavelengths allowed imaging of capillaries down to depths of ~250 µm (Supplementary Fig. 4).

1P light targeting with DMDs. We used optogenetic activation with blue light to selectively target either apical dendrites or cell bodies. Targeted 1 P illumination may spuriously activate CheRiff outside the focal plane. We attempted dendrite-targeted 2 P optogenetic stimulation to mitigate concern from off-target excitation. 2 P stimulation could evoke spikes when targeted to the soma but not when targeted to the dendrites, so this approach was not pursued. For targeted soma activation, we selected regions devoid of apical dendrites to prevent spurious dendritic stimulation. For voltage recordings, the orange light was meticulously confined to the recording sites, which led to a decrease in background fluorescence. The 594 nm illumination intensity was 25 mW mm^{-2} at the sample plane.

Imaging sessions. Imaging experiments started 3–4 weeks after the cranial window surgery. The FRET-based chemogenetic voltage indicator Voltron2 requires an organic dye to become fluorescent. We delivered the JFX608-HaloTag or JF608-HaloTag dye ligand[54] (100 µl, 1 mM) using retro-orbital injection at least 24 h before imaging. We did not observe a difference between the deuterated (JFX608) and non-deuterated (JF608) dyes, so data were pooled. We chose the JF608 dye because of its bioavailability, compatibility with the blue-shifted channelrhodopsin, its voltage sensitivity and the ability to image to depths of 200–300 µm with red light (Supplementary Fig. 4). Neurons remained labeled for up to 1 week. Illumination intensity was typically adjusted to produce a detected photon flux from the dendrite of ~900 photon $\mu m^{-2} ms^{-1}$. All imaging was performed with custom MATLAB/C^{++} acquisition software (www.luminosmicroscopy.com). We observed good imaging for up to 1 year after virus injection, eventually limited by scarring and regrowth of skull tissue under the window adapter.

Cell health validation. Cell health was assessed by the response of a cell to blue light steps of increasing intensity. This protocol activated the neuron and led to spiking rates correlated to the light intensity. We performed this validation before and after each imaging session.

Imaging-anesthetized animals. Imaging typically started 2–3 weeks after surgery. Mice were lightly anesthetized (0.7–1% isoflurane) and head-fixed under the upright microscope using a titanium head plate. Eyes were kept moist using ophthalmic eye ointment. The body temperature was continuously monitored and maintained at 37 °C using a heating pad (WPI). A typical imaging session lasted 2–3 h, after which the animals quickly recovered and were returned to their home cage.

Imaging awake animals. Head-fixed animals were imaged while awake on a custom-built motorized treadmill. Before imaging sessions started, mice were habituated to head restraint by training them every 24 h for 15–30 min. During each training session mice were first habituated to the head restraint until completely relaxed. Whisker stimulation was applied to the contralateral whiskers using an air puff of 100 ms and 45 psi (Picospritzer III, Parker), repeated every 4 s.

Data analysis

Three-dimensional motion correction. Transverse *xy* motion correction was performed by using a MATLAB implementation of NoRMCorre (https://github.com/flatironinstitute/NoRMCorre). For z-motion correction, before each imaging session a *z*-stack was acquired with axial displacements in steps of 1 µm, up to ±10 µm from the focal plane. After voltage imaging acquisition, each frame of the recording was cross-correlated to each frame of the reference *z*-stack to determine the axial displacement. By analysis of the total dendrite fluorescence as a function of the *z*-offset, we determined that there was negligible signal loss for displacements up to ±2.5 µm (Supplementary Fig. 6). Frames that deviated by more than ±2.5 µm in axial displacement were excluded from the analysis. In awake recordings, an average of 10 ± 6% of frames were discarded (mean ± s.d., $n = 5$ mice), with variability across animals depending on the quality of the head-mount, surgical preparation and animal activity. The movement-contaminated frames tended to come in a small number of discrete events (for example, when the mouse attempted to move its head), so these epochs were excluded from the analysis. All data during the valid recording epochs were included, provided that the analysis window did not extend into an excluded region.

Fluorescence signal extraction. Blood vessels were manually masked to avoid spurious fluorescence fluctuations. Movies were corrected for photobleaching by dividing the movie by an exponential fit of the mean fluorescence. The time-average image was then subtracted from each frame to create a movie of the deviations in fluorescence, $\Delta F(x,y,t)$. We created an 'activity image' $A(x,y)$ by calculating the autocovariance function of the fluorescence at each pixel and evaluating this function at a lag of one frame, that is, $A(x,y) = \langle \Delta F(x,y,t)\, \Delta F(x,y,t+dt) \rangle_t$, where dt is the inter-frame interval and $\langle \cdot \rangle_t$ indicates an average over time. This lag-1 autocovariance is similar to the variance except that it lacks contamination from the delta-function-correlated shot noise. The lag-1 autocovariance images clearly showed the dendritic morphology, indicating that the voltage fluctuations followed the shape of the dendrite.

We manually defined polygonal regions of interest (ROIs) around the individual dendritic branches. We avoided blood vessels, which otherwise contributed to uncorrectable noise. The movie of each ROI was independently processed with principal component analysis. Typically, the first principal component showed a spatial footprint which resembled the average fluorescence of the dendrite and whose time course clearly corresponded to neural activity. Other components had spatial footprints, with positive and negative regions indicating contributions from tissue motion or residual blood flow artifacts, and with temporal components that indicated contributions from breathing, heartbeat or high-frequency blood-flow-related speckle. Although principal component analysis is not guaranteed to isolate voltage signals from other sources of noise, we found that as a practical matter, this approach was highly effective (Supplementary Fig. 8). In most figures, we just show the manually defined bounding box of the ROI, not the full weight mask used to extract the voltage signal.

Spike detection. Spikes were detected using a custom threshold-based algorithm adapted from ref. 21. The raw fluorescence signal was first scanned for upward threshold crossings, defined as points where the signal rose above a user-defined threshold (Supplementary Fig. 16). For each such event, the algorithm identified the subsequent downward threshold crossing and located the local maximum within that interval, corresponding to the spike peak. To avoid overcounting closely spaced transients, any peaks separated by fewer than a minimum ISI were grouped into clusters; only the highest peak within each cluster was retained. This approach ensured that spike detections reflected discrete, well-separated events exceeding the defined amplitude criterion. All spike times were returned as indices corresponding to the time points of the detected peaks.

In cases where the signal-to-noise ratio was low (for example, very distal dendrite recordings), we validated the spike-detection setting a negative threshold an equal distance below the mean as the positive-going spike-detection threshold. The rate of events crossing the negative threshold indicated the false positive rate.

Event classification and amplitude measurement. bAPs were defined as events detected in both soma and dendrite. Local dendritic events were defined as dendritic events where the corresponding somatic depolarization was less than two standard deviations above the mean somatic baseline (Supplementary Fig. 16).

For the analyses of bAP amplitudes in Fig. 2, we first identified spike times at the soma. Using these event times as a trigger, we calculated STA waveforms for soma and dendrites. These waveforms were expressed as $\Delta F/F$, where F is the mean fluorescence from −20 to −13 frames before the spike, and ΔF is measured relative F. This timing was selected to be close enough to the spike to largely avoid contamination from preceding spikes but to be far enough before the spike to avoid contamination from brief subthreshold fluctuations immediately preceding the spike. The window for determining the fluorescence baseline was adjusted if either of these conditions was violated. We sought to avoid pre-spike subthreshold fluctuations in determining the baseline for ΔF because the biophysically relevant quantity is the voltage to which the spike reaches, not the change in voltage from the inflection point to the peak. Spike amplitude was defined as the maximum $\Delta F/F$ in a 10-ms window around the soma spike time; in some cases, a ±1-frame window around the peak was averaged to improve robustness to shot noise.

The amplitude of each individual bAP or local event was measured relative to the STA amplitude of the corresponding neuronal compartment. This normalization allows for comparison between dendrites of fluctuations in bAP transmission efficiency. The distribution of bAP amplitudes was unimodal, so the degree of attenuation was a continuous variable. The degree of bAP attenuation was always measured relative to a defined set of other bAPs, as specified in the text.

1P HiLo for morphology reconstruction. Three-dimensional mapping of neurons was performed using HiLo[24] at a succession of *z*-planes (Supplementary Fig. 10). Briefly, HiLo was implemented by using the DMD to alternately project random patterns of on and off pixels, and wide-field homogeneous illumination. These sets of images could be used to determine the relative contributions of in-focus and out-of-focus fluorescence at each pixel. The three-dimensional structural *z*-stack was imported to Neutube (https://neutracing.com/) and semiautomatic reconstruction was performed to obtain a neuron skeleton. The skeleton was used to find the dendrite–soma contour distance along the three-dimensional branch structure (Fig. 2) and to count the branch points (Supplementary Fig. 11). In some instances, we also performed 2 P structural microscopy to validate the 1 P reconstructions (Supplementary Video 1). The deepest recorded soma was located 230 µm below the pia. Basal dendrites were typically not resolved in our recordings.

Robust estimate of $\Delta F/F_0$. For the analysis of bAP amplitudes in Fig. 2, we created STA movies for the soma and dendrite planes, in all cases

triggering off the spike times at the soma. We defined ROIs that included the soma and dendrites. For each ROI, we calculated an image of the time-average fluorescence (F_0) and the frame-by-frame deviations in fluorescence (ΔF). For each frame, we then created a pixel-by-pixel scatterplot of F_0 versus ΔF. A linear regression to determine the slope of this line provided an estimate of $\Delta F/F_0$ (as the inverse slope; Supplementary Fig. 13). Spatially homogeneous background contributed to an offset in F_0, and out-of-focus signals contributed to an offset in ΔF, but neither of these quantities affected the slope of F_0 versus ΔF.

Shot-noise-robust estimates of variance and cross-correlation. Photon-shot-noise inflates the variance of an optical signal and deflates the cross-correlation of signals taken from nonoverlapping ROIs. However, the statistical independence of shot-noise in distinct pixels and time bins enables correction for these artifacts.

For a constant fluorescence source with mean photon counts Γ, the Poisson statistics of shot noise imply that the variance in the counts is also Γ. Thus, a variance image calculated from a movie of a static fluorescent sample reproduces the time-averaged image of the sample. If sample fluctuations last longer than one frame, then a shot-noise-robust estimate of sample variance can be calculated from the lag-1 autocovariance. Similarly, if sample fluctuations extend over more than one pixel, then a shot-noise-robust estimate of sample variance can be calculated via:

$$\mathrm{Var}\,(X) \cong \frac{1}{N-1}\sum_{t=0}^{N}(x_{\mathrm{even}}(t)-\bar{x}_{\mathrm{even}})\times(x_{\mathrm{odd}}(t)-\bar{x}_{\mathrm{odd}})$$

where x_{even} and x_{odd} correspond to the even and odd pixels in a checkerboard pattern of a given ROI (for example, Supplementary Fig. 15). The summation is for the N frames of the recording. This procedure was used for the variance calculations in Supplementary Fig. 8.

To estimate the contribution of photon-shot-noise to dendrite-to-dendrite cross-correlation, we took the ROI around each dendrite branch and split it into two signals calculated from the averages of two interleaved checkerboard patterns of pixels (Supplementary Fig. 15a). These two signals are expected to be nearly identical, except for statistically independent realizations of the photon-shot-noise. The cross-correlation of these reference signals set an upper bound on the expected cross-correlation between signals from distinct dendritic branches.

Analysis of bAP attenuation during spontaneous activity. We first found each spike at the soma and the corresponding events in each dendritic recording. For each dendritic compartment, we normalized bAPs according to their mean amplitude to allow analysis of variations in bAP amplitude within and between recording sites. ISIs were calculated at the soma and classified into 'accelerating' or 'decelerating' triplets. The amplitude of the third spike in each triplet was determined and was classified based on whether the preceding two ISIs were accelerating or decelerating.

Analysis of bAP attenuation during optogenetic stimulation. We first found all optogenetically evoked spikes at the soma and identified the corresponding events in the dendritic recordings. For each dendrite, bAP amplitudes were normalized according to the mean bAP amplitude in the final half (200–450 ms) of the stimulus period, a time when we observed that bAP amplitudes were stable in amplitude. We compared this epoch to the amplitude in the first 50 ms, when bAPs were relatively suppressed, and to the amplitude from 50 ms to 100 ms, when bAPs were relatively amplified. Spikes and their corresponding bAPs were sorted into time bins relative to the optogenetic stimulus onset. Within each time bin, we calculated an STA waveform at the soma and dendrites, triggered off the spike times at the soma and then calculated the mean amplitude of the bAP in each dendritic compartment. Dendritic compartments were assorted into groups based on the time delay between the peak of the soma spike and the peak of the local bAP. Mean bAP amplitudes were calculated for electrotonically proximal dendrites (conduction delay less than 3 ms) and for electrotonically distal dendrites (conduction delay more than 3 ms).

Statistics and reproducibility. No statistical method was used to predetermine sample sizes. Sample sizes were as large as could be practically acquired and are similar to those reported in previous publications. Only dendrites with a signal-to-noise ratio (spike height to baseline noise) greater than three were included in the analysis. Frames with axial motion greater than ±2.5 µm were excluded from the analysis, selected based on the optical depth of focus (see the 'Three-dimensional motion correction' section); no other data were excluded from the analyses. These exclusion criteria were pre-established. The experiments were not randomized because the research did not involve comparisons between groups of animals. Data collection and analysis were not performed blind to the conditions of the experiments. Statistical comparisons used nonparametric tests (two-sided Wilcoxon rank-sum and two-sided Wilcoxon signed-rank tests), which do not assume normality. Exact P values are reported where possible. No adjustments were made for multiple comparisons because statistical tests did not include multiple comparisons; 95% CIs were calculated using bootstrap resampling (1,000 iterations) unless otherwise stated.

Reporting summary

Further information on research design is available in the Nature Portfolio Reporting Summary linked to this article.

Data availability

The voltage imaging datasets used for Figs. 1–4 are on the DANDI archive under accession code 001791. Source data are provided with this paper.

Code availability

Data analysis was performed using scripts consisting of standard MATLAB functions. The analysis scripts are available from the corresponding author.

References

45. Jun-ichi, M. et al. Expression vector system based on the chicken β-actin promoter directs efficient production of interleukin-5. *Gene* **79**, 269–277 (1989).
46. Schnütgen, F. et al. A directional strategy for monitoring Cre-mediated recombination at the cellular level in the mouse. *Nat. Biotechnol.* **21**, 562–565 (2003).
47. Gradinaru, V. et al. Molecular and cellular approaches for diversifying and extending optogenetics. *Cell* **141**, 154–165 (2010).
48. Kim, J. H. et al. High cleavage efficiency of a 2A peptide derived from porcine teschovirus-1 in human cell lines, zebrafish and mice. *PLoS ONE* **6**, e18556 (2011).
49. Lim, S. T., Antonucci, D. E., Scannevin, R. H. & Trimmer, J. S. A novel targeting signal for proximal clustering of the Kv2.1 K^+ channel in hippocampal neurons. *Neuron* **25**, 385–397 (2000).
50. Adam, Y. et al. Voltage imaging and optogenetics reveal behaviour-dependent changes in hippocampal dynamics. *Nature* **569**, 413–417 (2019).
51. Goldey, G. J. et al. Removable cranial windows for long-term imaging in awake mice. *Nat. Protoc.* **9**, 2515–2538 (2014).
52. Judkewitz, B., Rizzi, M., Kitamura, K. & Häusser, M. Targeted single-cell electroporation of mammalian neurons in vivo. *Nat. Protoc.* **4**, 862–869 (2009).

53. Waters, J. Sources of widefield fluorescence from the brain. *eLife* **9**, e59841 (2020).
54. Lin, D. et al. Time-tagged ticker tapes for intracellular recordings. *Nat. Biotechnol.* **41**, 631–639 (2023).

Acknowledgements

We thank A. Preecha and S. Begum for technical assistance and B. Sabatini for helpful discussions. J.D.W.-C. acknowledges D. P. Ornelas-Huerta for useful discussions.

Author contributions

J.D.W.-C. developed the optical system, performed the cranial window surgeries and acquired and analyzed the data. P.P. developed the genetic constructs. P.P. and B.H.L. performed the in utero electroporations and cranial window surgeries. H.C.D. developed the instrument-control software. Y.Q. identified and characterized the dye and opsin combination for in vivo Optopatch-V. H.T. and D.K. helped with experiment design. D.G.I. performed the numerical simulations. J.B.G., S.E.P. and L.D.L. provided the HaloTag dyes and guidance on their use. A.E.C. supervised the project, helped with data analysis and wrote the paper along with J.D.W.-C.

Funding

This work was supported by a Vannevar Bush Faculty Fellowship N00014-18-1-2859; a Brain Research Foundation Scientific Innovations Award; the Harvard Brain Science Initiative; National Institutes of Health grant nos. R01-NS126043, R01-NS133755 and R01-MH117042; and a Chan Zuckerberg Initiative Dynamic Imaging grant no. 2023-321177. J.D.W.-C. is a Merck Awardee of the Life Sciences Research Foundation. J.B.G., S.E.P. and L.D.L. are supported by the Howard Hughes Medical Institute. The funders had no role in study design, data collection and analysis, decision to publish or preparation of the manuscript.

Competing interests

A.E.C. is a consultant to Quiver Biosciences and Exin Therapeutics and is a founder of Luminos LLC. L.D.L. is a scientific cofounder, shareholder and consultant of Eikon Therapeutics. US patent 9,933,417 describing azetidine-containing fluorophores and variant compositions (with L.D.L. as inventor) is assigned to the Howard Hughes Medical Institute. The other authors declare no competing interests.

Additional information

Supplementary information The online version contains supplementary material available at https://doi.org/10.1038/s41593-026-02339-4.

Correspondence and requests for materials should be addressed to Adam E. Cohen.

Peer review information *Nature Neuroscience* thanks Hillel Adesnik and the other, anonymous, reviewer(s) for their contribution to the peer review of this work.

nature portfolio

Corresponding author(s): Adam E Cohen

Last updated by author(s): Apr 17, 2026

Reporting Summary

Nature Portfolio wishes to improve the reproducibility of the work that we publish. This form provides structure for consistency and transparency in reporting. For further information on Nature Portfolio policies, see our Editorial Policies and the Editorial Policy Checklist.

Statistics

For all statistical analyses, confirm that the following items are present in the figure legend, table legend, main text, or Methods section.

n/a	Confirmed
☐	☒ The exact sample size (*n*) for each experimental group/condition, given as a discrete number and unit of measurement
☐	☒ A statement on whether measurements were taken from distinct samples or whether the same sample was measured repeatedly
☐	☒ The statistical test(s) used AND whether they are one- or two-sided *Only common tests should be described solely by name; describe more complex techniques in the Methods section.*
☐	☒ A description of all covariates tested
☐	☒ A description of any assumptions or corrections, such as tests of normality and adjustment for multiple comparisons
☐	☒ A full description of the statistical parameters including central tendency (e.g. means) or other basic estimates (e.g. regression coefficient) AND variation (e.g. standard deviation) or associated estimates of uncertainty (e.g. confidence intervals)
☐	☒ For null hypothesis testing, the test statistic (e.g. *F*, *t*, *r*) with confidence intervals, effect sizes, degrees of freedom and *P* value noted *Give P values as exact values whenever suitable.*
☒	☐ For Bayesian analysis, information on the choice of priors and Markov chain Monte Carlo settings
☒	☐ For hierarchical and complex designs, identification of the appropriate level for tests and full reporting of outcomes
☒	☐ Estimates of effect sizes (e.g. Cohen's *d*, Pearson's *r*), indicating how they were calculated

Our web collection on statistics for biologists contains articles on many of the points above.

Software and code

Policy information about availability of computer code

Data collection	Voltage imaging data was collected using a MATLAB (2019b, Mathworks) microscope control code (https://www.luminosmicroscopy.com).
Data analysis	All the analysis and statistical comparisons were performed with MATLAB (2019b, Mathworks) code using built-in functions.

For manuscripts utilizing custom algorithms or software that are central to the research but not yet described in published literature, software must be made available to editors and reviewers. We strongly encourage code deposition in a community repository (e.g. GitHub). See the Nature Portfolio guidelines for submitting code & software for further information.

Data

Policy information about availability of data

All manuscripts must include a data availability statement. This statement should provide the following information, where applicable:

- Accession codes, unique identifiers, or web links for publicly available datasets
- A description of any restrictions on data availability
- For clinical datasets or third party data, please ensure that the statement adheres to our policy

Voltage imaging datasets used for the main figures of this study are on the DANDI archive under the accession code 001791 and are available https://dandiarchive.org/dandiset/001791. Raw source data can be provided upon reasonable request.

Research involving human participants, their data, or biological material

Policy information about studies with human participants or human data. See also policy information about sex, gender (identity/presentation), and sexual orientation and race, ethnicity and racism.

Reporting on sex and gender	*Use the terms sex (biological attribute) and gender (shaped by social and cultural circumstances) carefully in order to avoid confusing both terms. Indicate if findings apply to only one sex or gender; describe whether sex and gender were considered in study design; whether sex and/or gender was determined based on self-reporting or assigned and methods used.* *Provide in the source data disaggregated sex and gender data, where this information has been collected, and if consent has been obtained for sharing of individual-level data; provide overall numbers in this Reporting Summary. Please state if this information has not been collected.* *Report sex- and gender-based analyses where performed, justify reasons for lack of sex- and gender-based analysis.*
Reporting on race, ethnicity, or other socially relevant groupings	*Please specify the socially constructed or socially relevant categorization variable(s) used in your manuscript and explain why they were used. Please note that such variables should not be used as proxies for other socially constructed/relevant variables (for example, race or ethnicity should not be used as a proxy for socioeconomic status).* *Provide clear definitions of the relevant terms used, how they were provided (by the participants/respondents, the researchers, or third parties), and the method(s) used to classify people into the different categories (e.g. self-report, census or administrative data, social media data, etc.)* *Please provide details about how you controlled for confounding variables in your analyses.*
Population characteristics	*Describe the covariate-relevant population characteristics of the human research participants (e.g. age, genotypic information, past and current diagnosis and treatment categories). If you filled out the behavioural & social sciences study design questions and have nothing to add here, write "See above."*
Recruitment	*Describe how participants were recruited. Outline any potential self-selection bias or other biases that may be present and how these are likely to impact results.*
Ethics oversight	*Identify the organization(s) that approved the study protocol.*

Note that full information on the approval of the study protocol must also be provided in the manuscript.

Field-specific reporting

Please select the one below that is the best fit for your research. If you are not sure, read the appropriate sections before making your selection.

☒ Life sciences ☐ Behavioural & social sciences ☐ Ecological, evolutionary & environmental sciences

For a reference copy of the document with all sections, see nature.com/documents/nr-reporting-summary-flat.pdf

Life sciences study design

All studies must disclose on these points even when the disclosure is negative.

Sample size	Experiments were performed in as many animals, cells, and dendrites as was practical.
Data exclusions	Data were excluded during epochs of substantial motion artifacts, as defined in the Methods. Only dendrites with a signal-to-noise ratio (spike height:baseline noise) > 3 were included in the analysis.
Replication	All experiments were replicated in at least n = 3 mice. All replication efforts were successful.
Randomization	All mice were subjected to the same measurement protocols, so there was no random assignment to groups.
Blinding	There was no assignment to groups, so blinding was not relevant.

Reporting for specific materials, systems and methods

We require information from authors about some types of materials, experimental systems and methods used in many studies. Here, indicate whether each material, system or method listed is relevant to your study. If you are not sure if a list item applies to your research, read the appropriate section before selecting a response.

Materials & experimental systems

n/a	Involved in the study
☐	☐ Antibodies
☐	☐ Eukaryotic cell lines
☐	☐ Palaeontology and archaeology
☐	☒ Animals and other organisms
☐	☐ Clinical data
☐	☐ Dual use research of concern
☐	☐ Plants

Methods

n/a	Involved in the study
☐	☐ ChIP-seq
☐	☐ Flow cytometry
☐	☐ MRI-based neuroimaging

Antibodies

Antibodies used: *Describe all antibodies used in the study; as applicable, provide supplier name, catalog number, clone name, and lot number.*

Validation: *Describe the validation of each primary antibody for the species and application, noting any validation statements on the manufacturer's website, relevant citations, antibody profiles in online databases, or data provided in the manuscript.*

Eukaryotic cell lines

Policy information about cell lines and Sex and Gender in Research

Cell line source(s): *State the source of each cell line used and the sex of all primary cell lines and cells derived from human participants or vertebrate models.*

Authentication: *Describe the authentication procedures for each cell line used OR declare that none of the cell lines used were authenticated.*

Mycoplasma contamination: *Confirm that all cell lines tested negative for mycoplasma contamination OR describe the results of the testing for mycoplasma contamination OR declare that the cell lines were not tested for mycoplasma contamination.*

Commonly misidentified lines (See ICLAC register): *Name any commonly misidentified cell lines used in the study and provide a rationale for their use.*

Palaeontology and Archaeology

Specimen provenance: *Provide provenance information for specimens and describe permits that were obtained for the work (including the name of the issuing authority, the date of issue, and any identifying information). Permits should encompass collection and, where applicable, export.*

Specimen deposition: *Indicate where the specimens have been deposited to permit free access by other researchers.*

Dating methods: *If new dates are provided, describe how they were obtained (e.g. collection, storage, sample pretreatment and measurement), where they were obtained (i.e. lab name), the calibration program and the protocol for quality assurance OR state that no new dates are provided.*

☐ Tick this box to confirm that the raw and calibrated dates are available in the paper or in Supplementary Information.

Ethics oversight: *Identify the organization(s) that approved or provided guidance on the study protocol, OR state that no ethical approval or guidance was required and explain why not.*

Note that full information on the approval of the study protocol must also be provided in the manuscript.

Animals and other research organisms

Policy information about studies involving animals; ARRIVE guidelines recommended for reporting animal research, and Sex and Gender in Research

Laboratory animals: Male and female adult mice (P50-P120) were used in experiments. The CD1 IGS mouse strain was used for all experiments.

Wild animals: No wild animals were used in this study.

Reporting on sex: Findings apply to both sexes.

Field-collected samples: No samples were collected in the field.

Ethics oversight	All procedures involving animals were in accordance with the National Institutes of Health Guide for the Care and Use of Laboratory Animals and were approved by the Harvard University Institutional Animal Care and Use Committee (IACUC).

Note that full information on the approval of the study protocol must also be provided in the manuscript.

Clinical data

Policy information about clinical studies

All manuscripts should comply with the ICMJE guidelines for publication of clinical research and a completed CONSORT checklist must be included with all submissions.

Clinical trial registration	*Provide the trial registration number from ClinicalTrials.gov or an equivalent agency.*
Study protocol	*Note where the full trial protocol can be accessed OR if not available, explain why.*
Data collection	*Describe the settings and locales of data collection, noting the time periods of recruitment and data collection.*
Outcomes	*Describe how you pre-defined primary and secondary outcome measures and how you assessed these measures.*

Dual use research of concern

Policy information about dual use research of concern

Hazards

Could the accidental, deliberate or reckless misuse of agents or technologies generated in the work, or the application of information presented in the manuscript, pose a threat to:

No	Yes	
☒	☐	Public health
☒	☐	National security
☒	☐	Crops and/or livestock
☒	☐	Ecosystems
☒	☐	Any other significant area

Experiments of concern

Does the work involve any of these experiments of concern:

No	Yes	
☒	☐	Demonstrate how to render a vaccine ineffective
☒	☐	Confer resistance to therapeutically useful antibiotics or antiviral agents
☒	☐	Enhance the virulence of a pathogen or render a nonpathogen virulent
☒	☐	Increase transmissibility of a pathogen
☒	☐	Alter the host range of a pathogen
☒	☐	Enable evasion of diagnostic/detection modalities
☒	☐	Enable the weaponization of a biological agent or toxin
☒	☐	Any other potentially harmful combination of experiments and agents

Plants

Seed stocks	*Report on the source of all seed stocks or other plant material used. If applicable, state the seed stock centre and catalogue number. If plant specimens were collected from the field, describe the collection location, date and sampling procedures.*
Novel plant genotypes	*Describe the methods by which all novel plant genotypes were produced. This includes those generated by transgenic approaches, gene editing, chemical/radiation-based mutagenesis and hybridization. For transgenic lines, describe the transformation method, the number of independent lines analyzed and the generation upon which experiments were performed. For gene-edited lines, describe the editor used, the endogenous sequence targeted for editing, the targeting guide RNA sequence (if applicable) and how the editor was applied.*
Authentication	*Describe any authentication procedures for each seed stock used or novel genotype generated. Describe any experiments used to assess the effect of a mutation and, where applicable, how potential secondary effects (e.g. second site T-DNA insertions, mosiacism, off-target gene editing) were examined.*

ChIP-seq

Data deposition

☐ Confirm that both raw and final processed data have been deposited in a public database such as GEO.

☐ Confirm that you have deposited or provided access to graph files (e.g. BED files) for the called peaks.

Data access links *May remain private before publication.*	*For "Initial submission" or "Revised version" documents, provide reviewer access links. For your "Final submission" document, provide a link to the deposited data.*
Files in database submission	*Provide a list of all files available in the database submission.*
Genome browser session (e.g. UCSC)	*Provide a link to an anonymized genome browser session for "Initial submission" and "Revised version" documents only, to enable peer review. Write "no longer applicable" for "Final submission" documents.*

Methodology

Replicates	*Describe the experimental replicates, specifying number, type and replicate agreement.*
Sequencing depth	*Describe the sequencing depth for each experiment, providing the total number of reads, uniquely mapped reads, length of reads and whether they were paired- or single-end.*
Antibodies	*Describe the antibodies used for the ChIP-seq experiments; as applicable, provide supplier name, catalog number, clone name, and lot number.*
Peak calling parameters	*Specify the command line program and parameters used for read mapping and peak calling, including the ChIP, control and index files used.*
Data quality	*Describe the methods used to ensure data quality in full detail, including how many peaks are at FDR 5% and above 5-fold enrichment.*
Software	*Describe the software used to collect and analyze the ChIP-seq data. For custom code that has been deposited into a community repository, provide accession details.*

Flow Cytometry

Plots

Confirm that:

☐ The axis labels state the marker and fluorochrome used (e.g. CD4-FITC).

☐ The axis scales are clearly visible. Include numbers along axes only for bottom left plot of group (a 'group' is an analysis of identical markers).

☐ All plots are contour plots with outliers or pseudocolor plots.

☐ A numerical value for number of cells or percentage (with statistics) is provided.

Methodology

Sample preparation	*Describe the sample preparation, detailing the biological source of the cells and any tissue processing steps used.*
Instrument	*Identify the instrument used for data collection, specifying make and model number.*
Software	*Describe the software used to collect and analyze the flow cytometry data. For custom code that has been deposited into a community repository, provide accession details.*
Cell population abundance	*Describe the abundance of the relevant cell populations within post-sort fractions, providing details on the purity of the samples and how it was determined.*
Gating strategy	*Describe the gating strategy used for all relevant experiments, specifying the preliminary FSC/SSC gates of the starting cell population, indicating where boundaries between "positive" and "negative" staining cell populations are defined.*

☐ Tick this box to confirm that a figure exemplifying the gating strategy is provided in the Supplementary Information.

Magnetic resonance imaging

Experimental design

Design type	*Indicate task or resting state; event-related or block design.*

Design specifications

Specify the number of blocks, trials or experimental units per session and/or subject, and specify the length of each trial or block (if trials are blocked) and interval between trials.

Behavioral performance measures

State number and/or type of variables recorded (e.g. correct button press, response time) and what statistics were used to establish that the subjects were performing the task as expected (e.g. mean, range, and/or standard deviation across subjects).

Acquisition

Imaging type(s)

Specify: functional, structural, diffusion, perfusion.

Field strength

Specify in Tesla

Sequence & imaging parameters

Specify the pulse sequence type (gradient echo, spin echo, etc.), imaging type (EPI, spiral, etc.), field of view, matrix size, slice thickness, orientation and TE/TR/flip angle.

Area of acquisition

State whether a whole brain scan was used OR define the area of acquisition, describing how the region was determined.

Diffusion MRI ☐ Used ☐ Not used

Preprocessing

Preprocessing software

Provide detail on software version and revision number and on specific parameters (model/functions, brain extraction, segmentation, smoothing kernel size, etc.).

Normalization

If data were normalized/standardized, describe the approach(es): specify linear or non-linear and define image types used for transformation OR indicate that data were not normalized and explain rationale for lack of normalization.

Normalization template

Describe the template used for normalization/transformation, specifying subject space or group standardized space (e.g. original Talairach, MNI305, ICBM152) OR indicate that the data were not normalized.

Noise and artifact removal

Describe your procedure(s) for artifact and structured noise removal, specifying motion parameters, tissue signals and physiological signals (heart rate, respiration).

Volume censoring

Define your software and/or method and criteria for volume censoring, and state the extent of such censoring.

Statistical modeling & inference

Model type and settings

Specify type (mass univariate, multivariate, RSA, predictive, etc.) and describe essential details of the model at the first and second levels (e.g. fixed, random or mixed effects; drift or auto-correlation).

Effect(s) tested

Define precise effect in terms of the task or stimulus conditions instead of psychological concepts and indicate whether ANOVA or factorial designs were used.

Specify type of analysis: ☐ Whole brain ☐ ROI-based ☐ Both

Statistic type for inference

Specify voxel-wise or cluster-wise and report all relevant parameters for cluster-wise methods.

(See Eklund et al. 2016)

Correction

Describe the type of correction and how it is obtained for multiple comparisons (e.g. FWE, FDR, permutation or Monte Carlo).

Models & analysis

n/a	Involved in the study
☐	☐ Functional and/or effective connectivity
☐	☐ Graph analysis
☐	☐ Multivariate modeling or predictive analysis

Functional and/or effective connectivity

Report the measures of dependence used and the model details (e.g. Pearson correlation, partial correlation, mutual information).

Graph analysis

Report the dependent variable and connectivity measure, specifying weighted graph or binarized graph, subject- or group-level, and the global and/or node summaries used (e.g. clustering coefficient, efficiency, etc.).

Multivariate modeling and predictive analysis

Specify independent variables, features extraction and dimension reduction, model, training and evaluation metrics.

nature neuroscience

Supplementary information

https://doi.org/10.1038/s41593-026-02339-4

Voltage dynamics of cortical dendrites in vivo

In the format provided by the authors and unedited

Supplementary movie captions

Movie 1: Comparison of 2P and HiLo z-stacks. A neuron was imaged twice, once via two-photon microscopy, and once via 1-photon structured illumination HiLo imaging. The 1P imaging was with an excitation wavelength of 594 nm and collection between 608-682 nm (Chroma, ET645/75m). The movie shows side-by-side z-stacks taken in the two modalities. Related to Fig. 1.

Movie 2: Reconstruction of a back-propagating action potential. A three-dimensional skeleton of the neuron was reconstructed from the HiLo z-stack, and the spike-triggered average waveform (triggered off the soma spike times) was plotted at the location of each recording site. Related to Fig. 2.

Supplementary figures

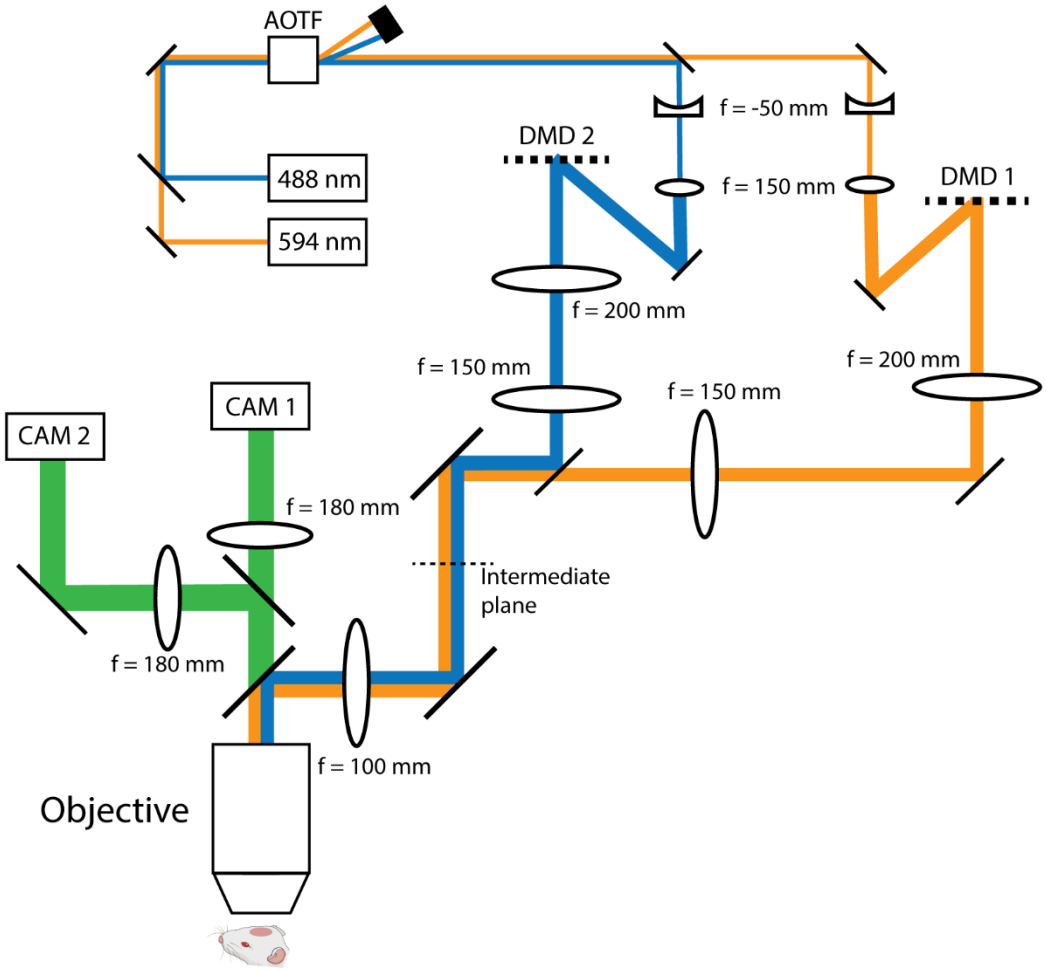

Figure S1. Optical layout. 488 and 594 nm light was amplitude modulated by an acousto-optic tunable filter (AOTF) and expanded by a 1:3 telescope. Blue and orange light illuminated two separate digital micromirror devices (DMDs). The images from the DMDs were combined and reimaged at an intermediate plane, and then relayed to the sample. Fluorescence (green) was redirected by a 50:50 beam splitter to two cameras. Adjustment of the tube lenses (f = 180 mm) allowed independent control of the imaging plane and field of view of each camera.

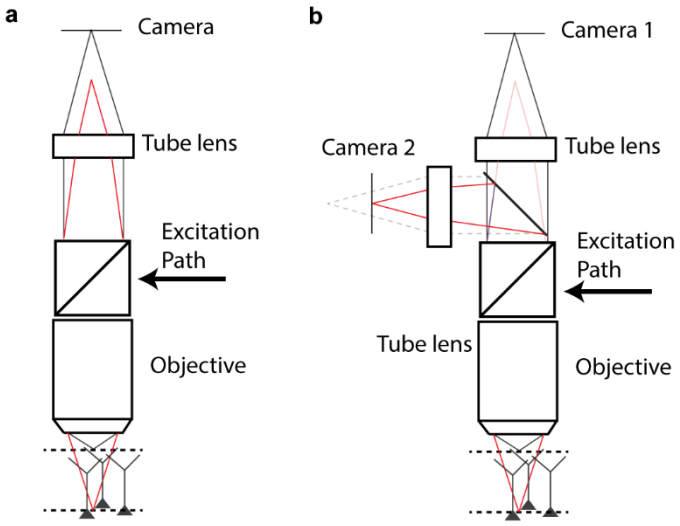

Figure S2. Simultaneous 1P imaging of two focal planes. a, Light from the soma couples to the objective and is reimaged at a different focal plane, located closer to the objective (Red). **b,** By adding a beam splitter, we image this plane to a second camera, allowing simultaneous recordings of somas and dendrites.

NOTES
1. MATERIAL: 316L SS
2. UNITS IN MILLIMETERS

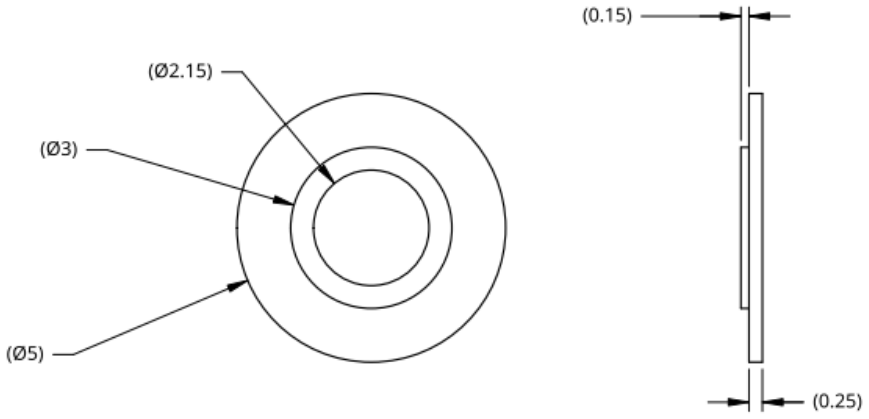

Figure S3. Stainless steel adapter. A cover slip of 3 mm diameter and 150 µm thickness was glued to the inner ring of 3 - 2.15 mm diameter. The combination of adapter and coverslip thicknesses spanned the skull, so the coverslip was in contact with the brain. By avoiding the need to glue multiple coverslips together, the glass thickness was kept at the optimum coverslip thickness for the objective lens. This approach minimized spherical aberrations. All units are in millimeters.

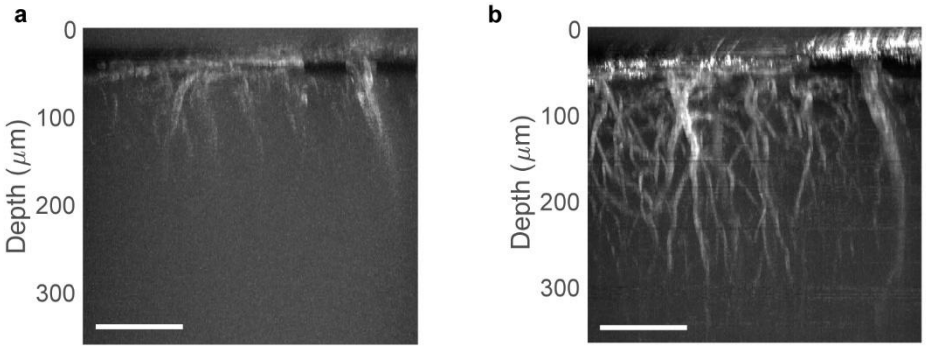

Figure S4. Wavelength-dependent penetration depth of one-photon structured illumination imaging. Side projection of one-photon z-stacks of labeled blood vessels acquired via HiLo. Images show the same sample and field of view, labeled with two different dyes. **a,** Imaging at 488 nm and **b,** Imaging at 635 nm. Scale bar 100 µm.

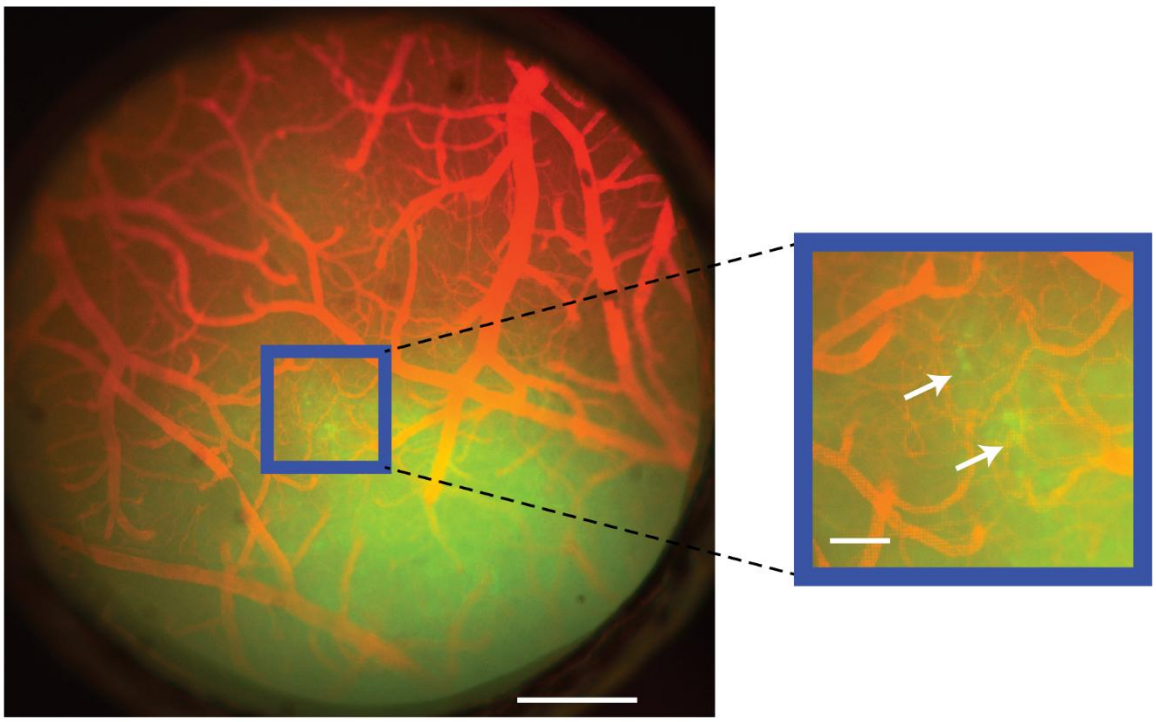

Figure S5. Blood vessel tracking. Blood vessel visualization was performed by injecting a fluorescent tracer. Scale bar 500 µm. We avoided recordings close to capillaries due to increased noise caused by scattering of flowing blood cells. Red: blood vessels, green: voltage indicator. Inset: Zoom in and arrows showing somas. Scale bar 250 µm.

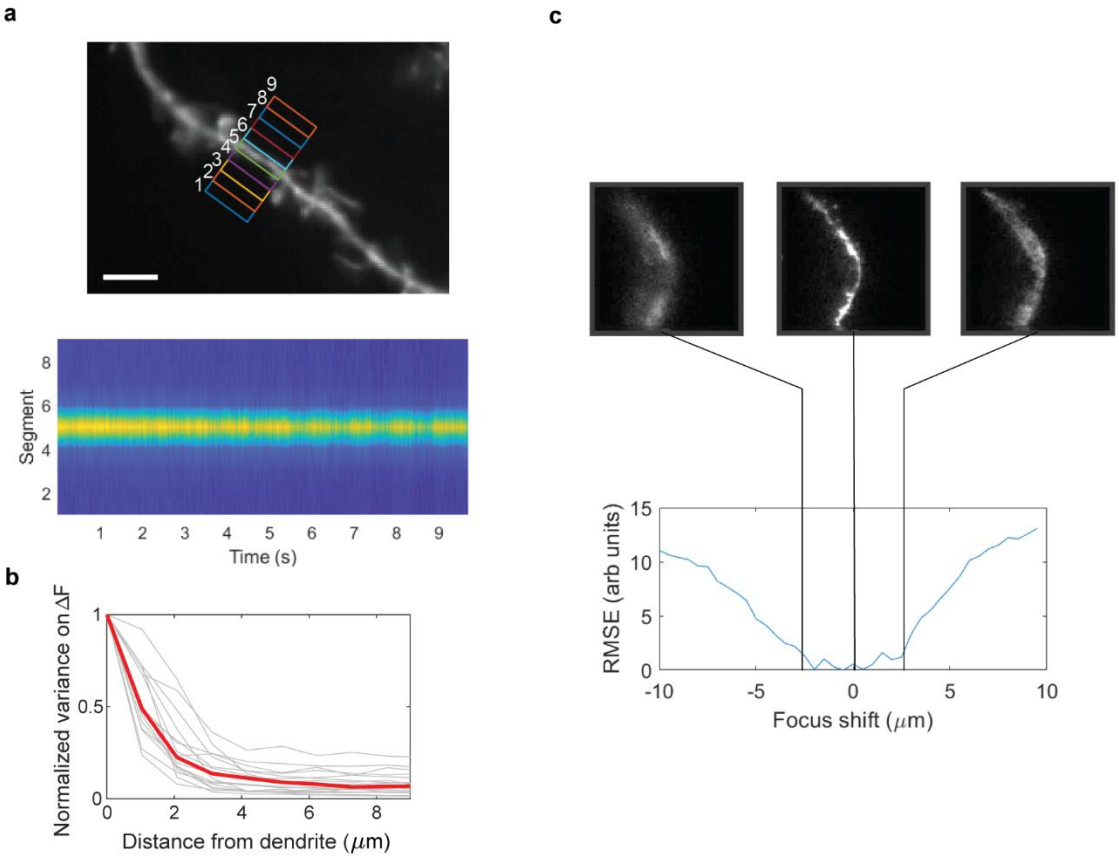

Figure S6. Signal localization in one-photon structured illumination microscopy *in vivo*. a, Procedure for measuring spatial localization and temporal stability of fluorescence from a dendrite. A region transverse to a dendrite was divided into 9 segments of 1.25 μm width (top) and the fluorescence in each region was measured vs. time (bottom), to characterize the in-focus and out-of-focus contributions to the signal. Scale bar 5 μm. **b,** Relative signal variance as a function of transverse offset from the dendrite. The variance decayed by 50% within 1 μm offset, and at 4 μm was only 9.0 ± 6.2% (mean ± s.d., *n* = 14 branches, 10 cells). Red line is the sample median. Here, variance was estimated in a shot-noise-insensitive procedure using the checkerboard pixel-selection shown in Fig. S13. **c,** Axial signal localization. For axial motion correction, we first acquired a z-stack of images of the dendrite (top). We then computed the root mean square error (RMSE) of each plane of the z-stack relative to the in-focus image, yielding a depth of focus ±2.5 μm (bottom). Each frame of the functional recording was then compared against the z-stack to determine the axial offset. Frames with > ±2.5 μm shift were excluded from analysis.

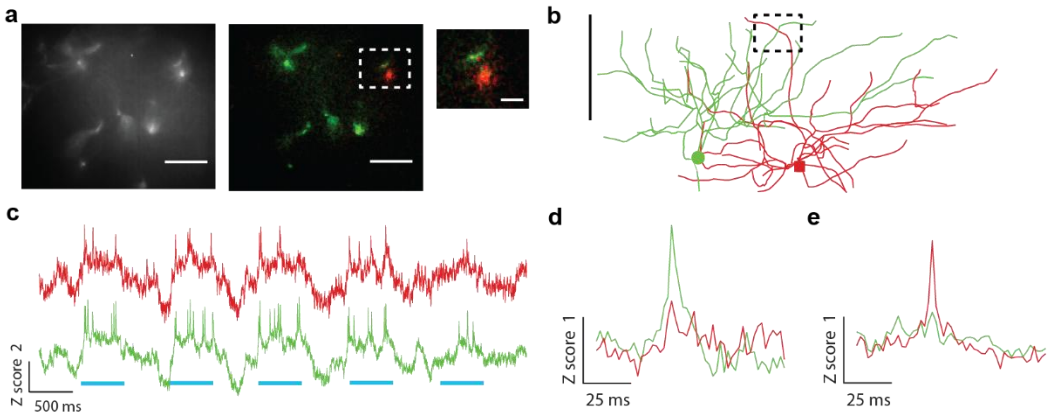

Figure S7. Dendrites from nearby neurons show minimal crosstalk in optical voltage recordings. a, Left: recording plane showing apical dendrites from two neurons co-labeled with a soma-targeted channelrhodopsin and broadly trafficked Voltron2. Scale bar 20 μm. Right: pixel-wise cross correlation with the spiking dynamics from Dendrite A (green) and Dendrite B (red) in the highlighted region. Many branches show correlated signal with Dendrite A, while the signal from Dendrite B is only correlated with itself. Inset scale bar is 5 μm. **b,** Side view of three-dimensional reconstructions of both neurons. The dotted black rectangle depicts the marked area in **a**. Scale bar 100 μm. **c,** Voltage traces from the red and green branches. **d–e,** Spike-triggered averages for both neurons, computed for events detected in either (d) Dendrite A or (e) Dendrite B.

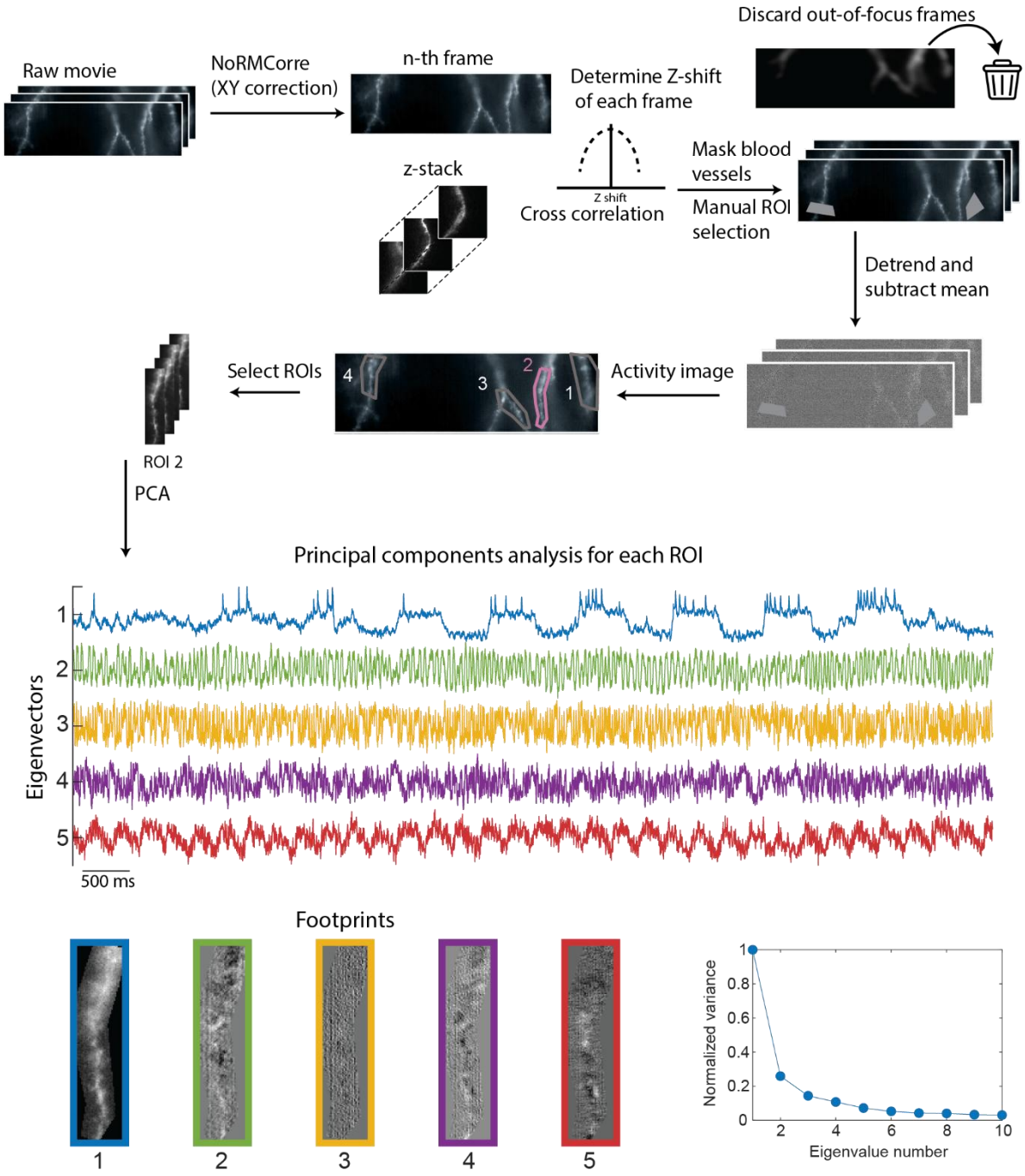

Figure S8. Signal extraction pipeline. Raw movies were corrected for transverse (XY) motion by rigid image registration and for axial (z) motion by cross-correlation to a previously acquired z-stack (Methods). Frames with axial shifts > ±2.5 μm were excluded from analysis. Blood vessels were manually masked, and the movie was detrended to correct for photobleaching. The time-average image was subtracted from each frame. We created an 'activity image' by multiplying the resulting movie with a one frame delayed version of itself, and then averaging over time (lag-1 autocorrelation; Methods). This procedure highlighted fluctuating parts of the movie and removed static bright regions. We then selected ROIs corresponding to dendrites. PCA within

each dendrite ROI revealed that the dominant signal component had a time-trace which corresponded to neural activity and a spatial footprint which corresponded to the average image of the dendrite fluorescence. Higher PCs had much smaller amplitudes, had timecourses which corresponded to motion artifacts or blood flow-induced speckle, and had spatial footprints which clearly did not correspond to whole-dendrite modulation of fluorescence.

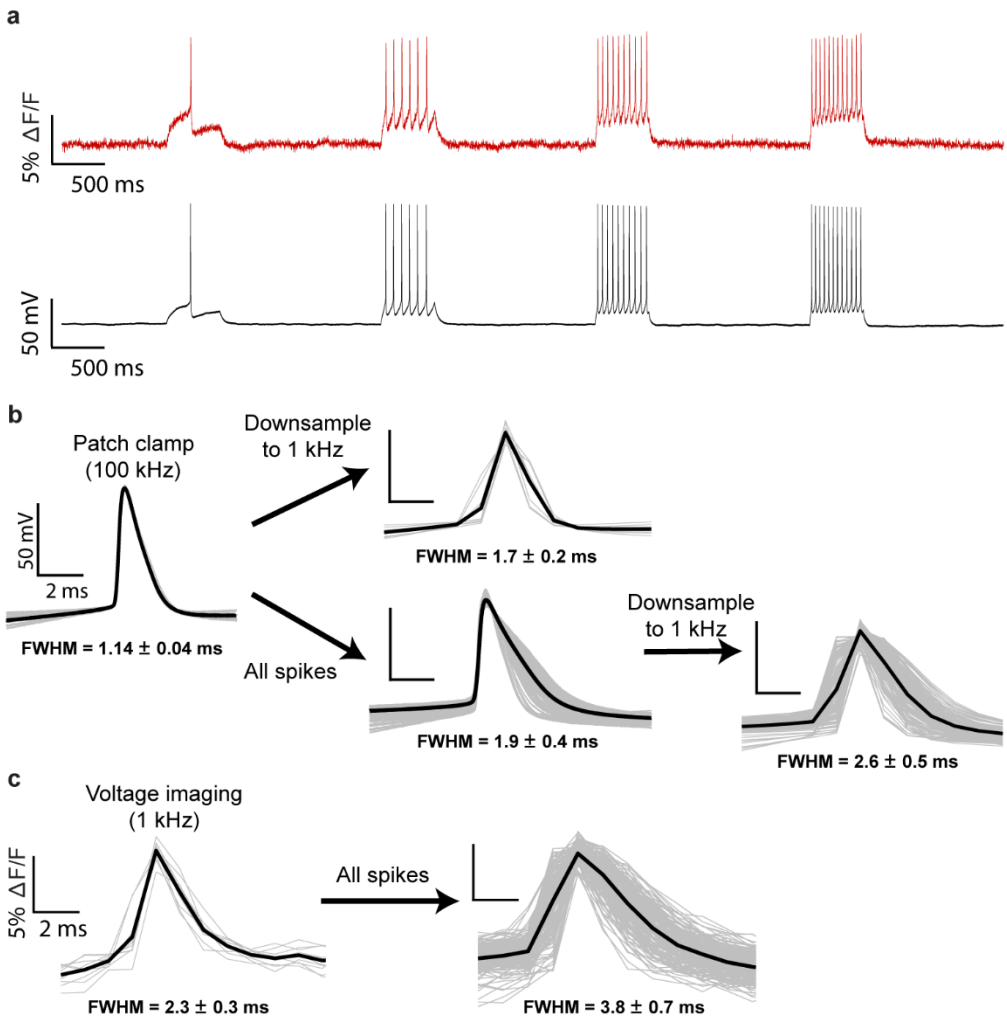

Figure S9. Validation by patch clamp in acute slices. a, Simultaneous optical and electrical recording showing the high fidelity of the voltage imaging measurements. **b**, Time budget for electrical recordings. Left: spike-triggered average of isolated spikes recorded by patch clamp (100 kHz) showed a FWHM of 1.14 ms. Downsampling the patch clamp data to 1 kHz increased the FWHM to 1.7 ms. High-frequency spikes driven by strong stimulation were broader than isolated spikes, so the STA over all spikes was broader (1.9 ms) than the STA of isolated spikes; and downsampling to 1 kHz further broadened the STA (2.6 ms). **c,** Time budget for optical recordings. Left: spike-triggered average of isolated spikes recorded by fluorescence (1 kHz) showed a FWHM of 2.3 ms. Compared to the 1 kHz downsampled patch clamp recording, the difference in FWHM is attributed to the 0.7 ms response time of Voltron2. Right: As with the patch clamp data, averaging over all spikes broadened the FWHM to 3.8 ms.

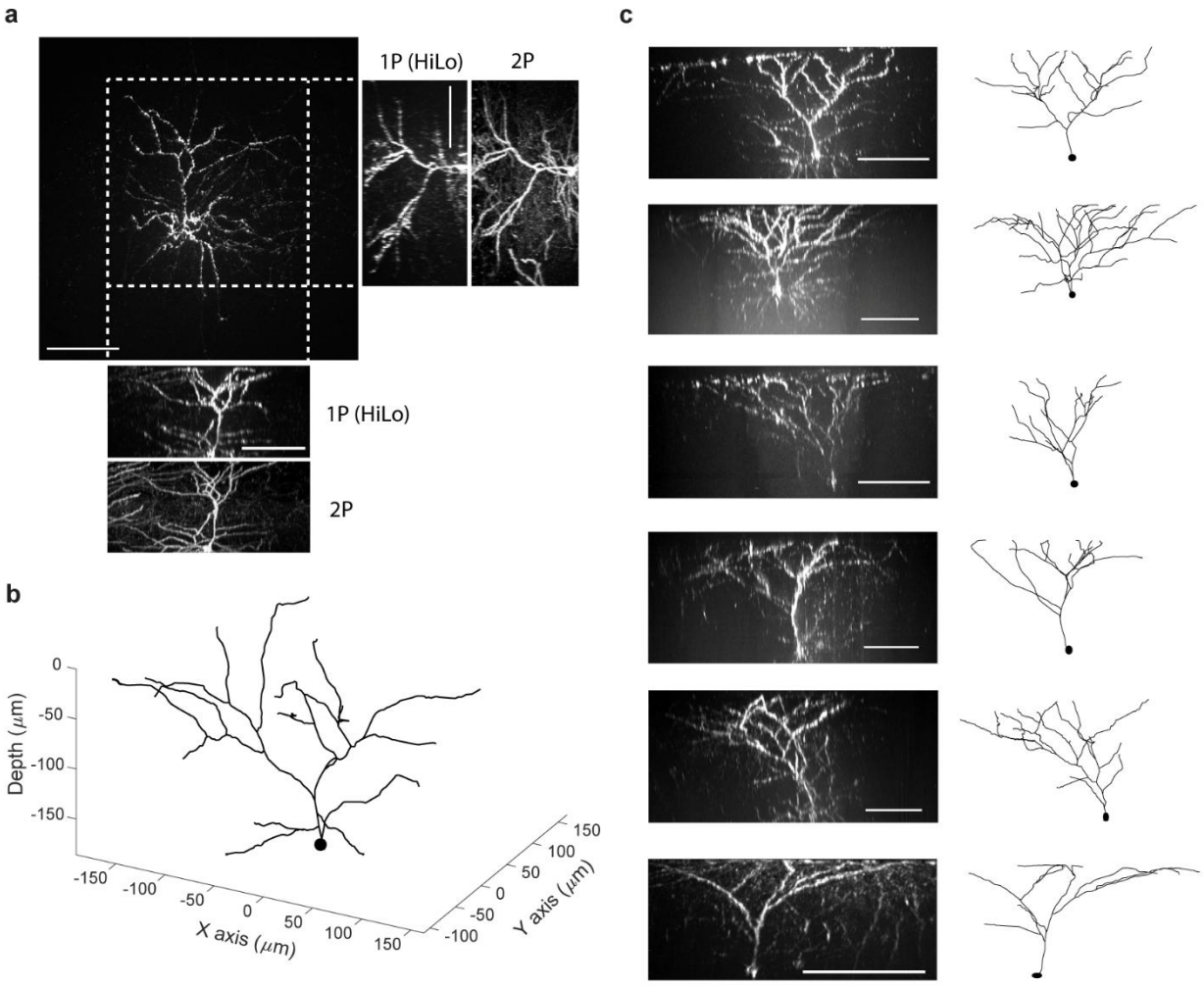

Figure S10. Three-dimensional reconstructions of individual neurons. a, A single L2/3 neuron imaged as a z-stack via 1P HiLo and 2P microscopies. Views show top (HiLo only) and side-view (HiLo and 2P) maximum-intensity projections (See also Supplemental movie S1). **b,** Three-dimensional skeleton reconstruction of the same neuron as (**a**). We selected neurons that were well isolated in a volume of 500×500×250 μm. **c,** Example HiLo z-stacks and reconstructions of apical dendritic arbors for 6 neurons. All scale bars 100 μm.

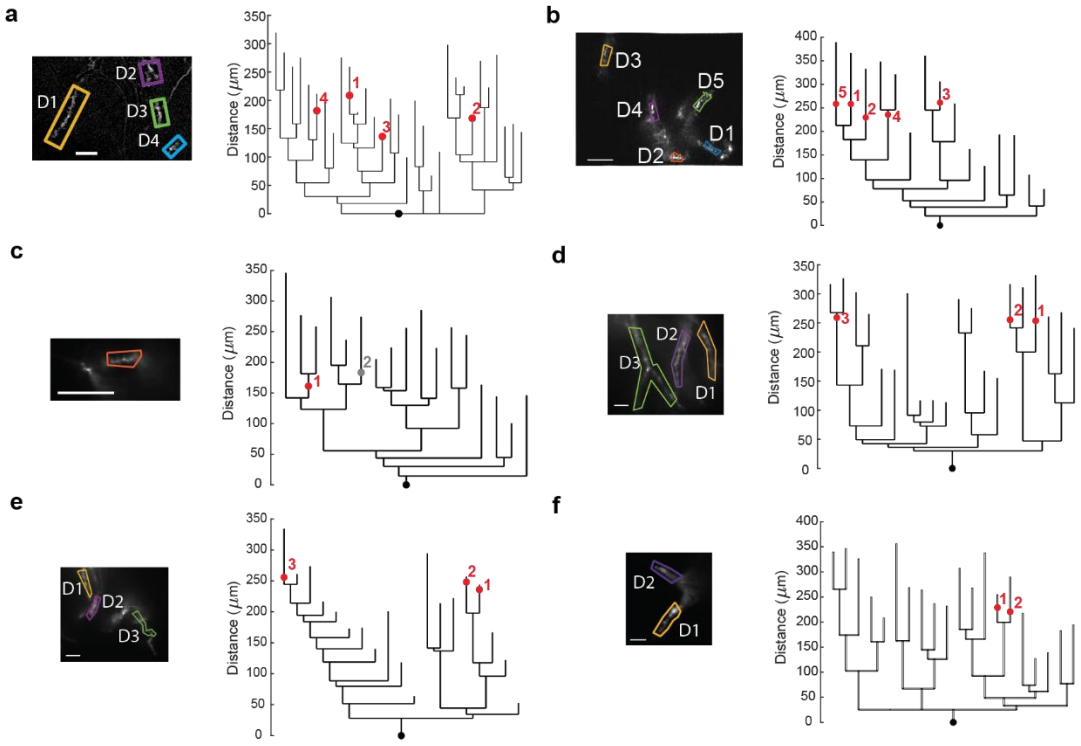

Figure S11. Dendrograms showing recording sites corresponding to Main Text figure panels. The corresponding main text figure panels are **a,** 1d-g; **b,** 3a-c; **c,** 3e-h; **d,** 4a-c; **e,** 4e-g; **f,** 4i-k.

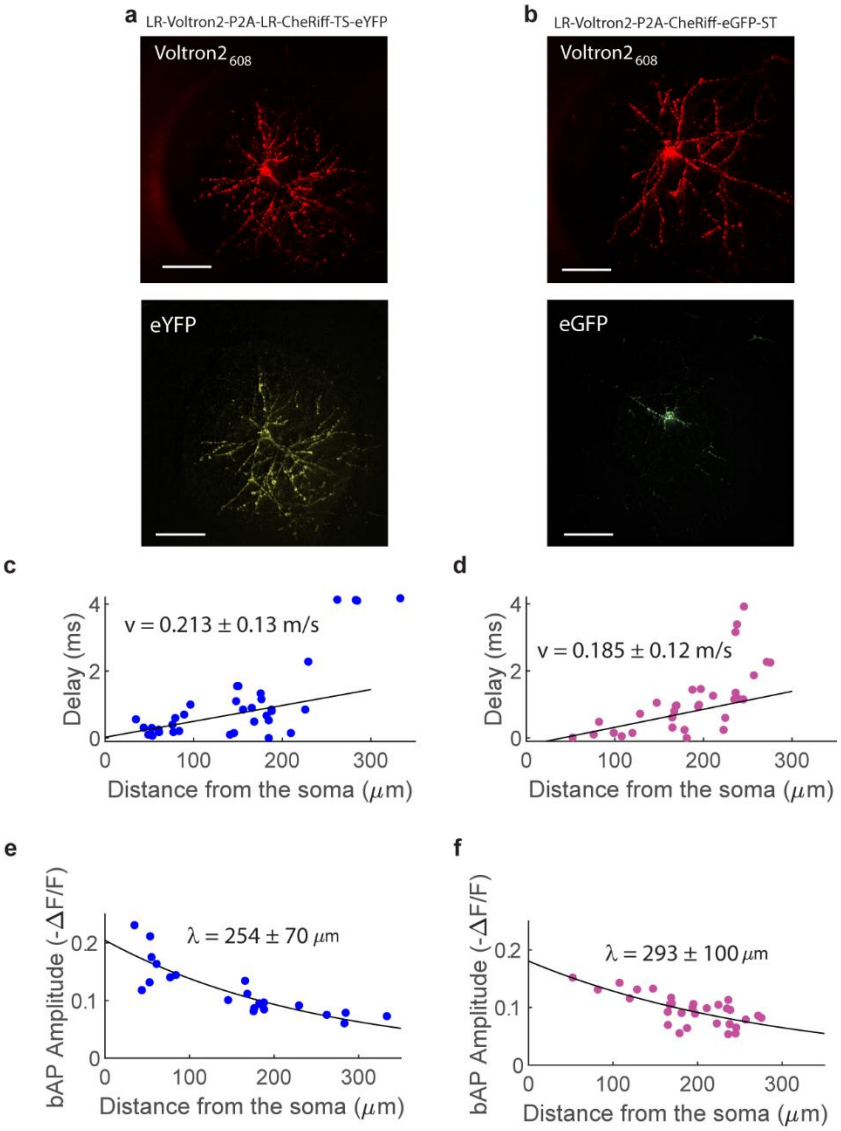

Figure S12. Comparison of backpropagation with broadly trafficked vs. soma-targeted channelrhodopsin. a, L2/3 pyramidal neuron with widely trafficked Voltron2 (top, red) and widely trafficked CheRiff-eYFP (bottom, yellow). Images show maximum-intensity projections of HiLo z-stacks at planes close to the soma. Scale bars 30 μm. **b,** L2/3 pyramidal neuron with widely trafficked Voltron2 (top, red) and CheRiff-eGFP targeted to the soma via the $K_V2.1$ soma-targeting (ST) motif (bottom, green). **c,d,** Comparison of bAP peak delay vs. distance from the soma, measured with non-soma targeted (c) and soma-targeted (d) CheRiff (p = 0.25, two-sample Kolmogorov-Smirnov test). **e**,**f,** Comparison of bAP amplitude vs. distance from the soma, measured with non-soma targeted (e) and soma-targeted (f) CheRiff (p = 0.35, two-sample Kolmogorov-Smirnov test). n = 37 dendrites, 6 neurons and 6 mice for the soma targeted experiments and 32 dendrites, 6 neurons, 6 mice for the widely trafficked. Recordings were taken at 1 kHz.

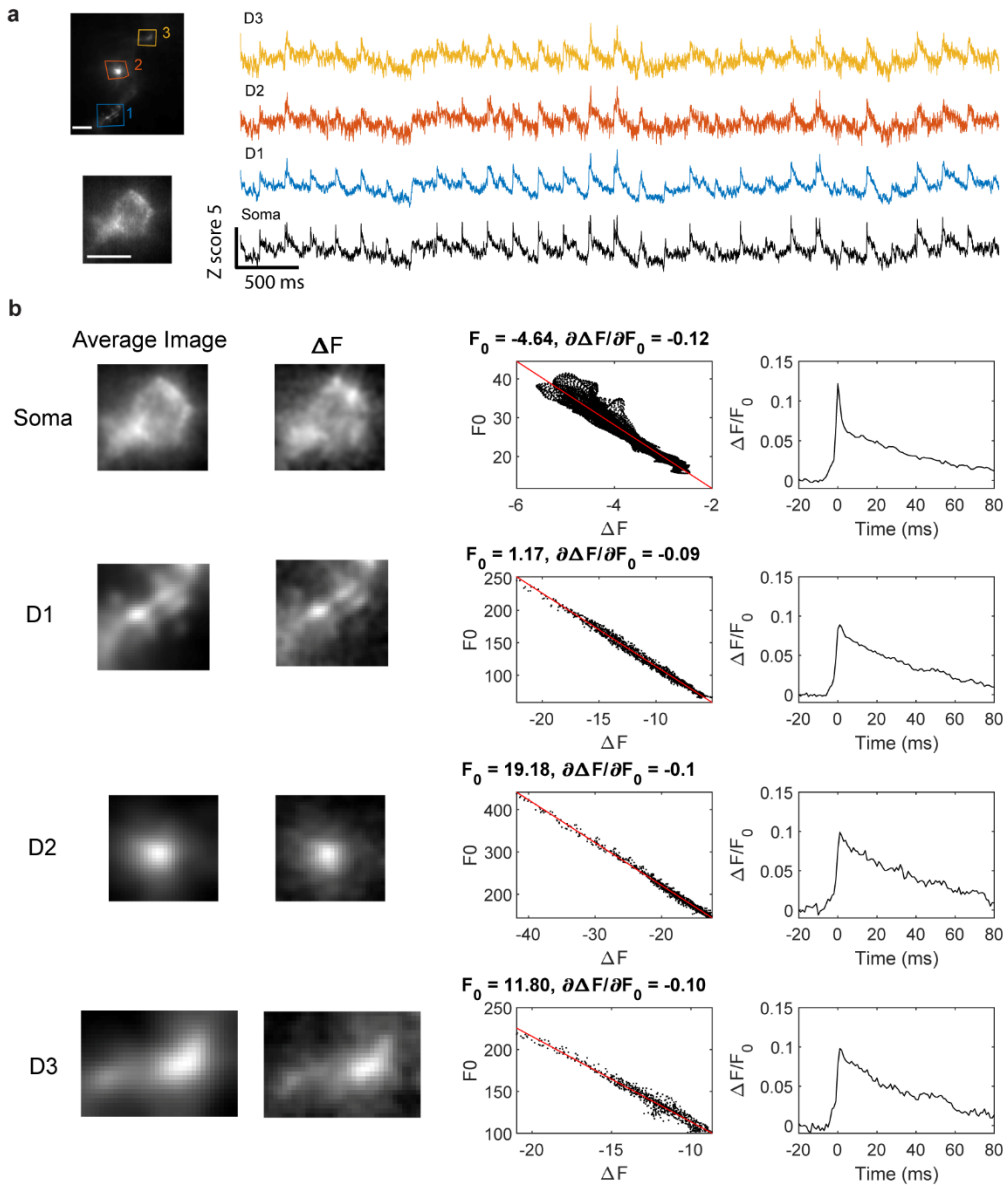

Figure S13. Robust calculation of ΔF/F$_0$. **a,** Backpropagating action potentials were evoked by targeted optogenetic stimulation of the soma. Fluorescence dynamics were simultaneously recorded at the soma and dendrites. A spike-triggered average movie (triggered off the somatic spike times) was calculated for each ROI. Scale bars 10 μm. **b,** The time-average image (F$_0$) of each ROI contained contributions from membrane-bound voltage-sensitive indicator molecules, and also possibly contributions from internalized voltage-insensitive indicators and from out-of-focus autofluorescence. The ΔF images were calculated frame-by-frame and comprise deviations in intensity from F$_0$. For each frame, a pixel-wise scatterplot of F$_0$ vs. ΔF was fit to a line via linear regression. The inverse of the slope is -ΔF/F$_0$. Constant background contributed to an offset in F$_0$, and out-of-focus voltage dynamics contributed to an offset in ΔF, but neither quantity affected the slope of F$_0$ vs. ΔF. Recordings were taken at 500 Hz.

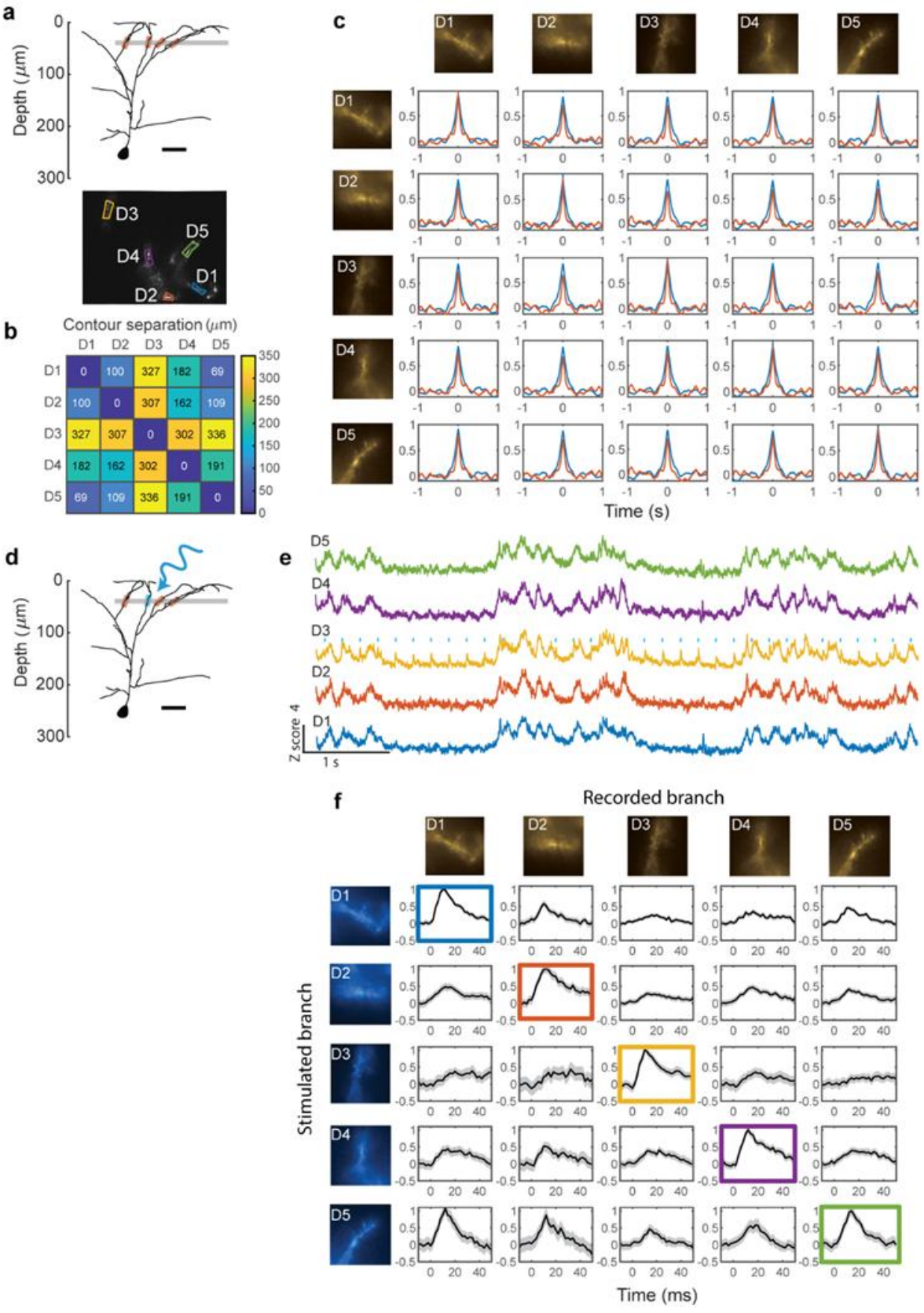
a
Depth (μm)
0
100
200
300
D3
D5
D4
D1
D2
b
Contour separation (μm)
D1 D2 D3 D4 D5
D1 0 100 327 182 69
D2 100 0 307 162 109
D3 327 307 0 302 336
D4 182 162 302 0 191
D5 69 109 336 191 0
350
300
250
200
150
100
50
0
c
D1
D2
D3
D4
D5
Time (s)
d
Depth (μm)
0
100
200
300
e
D5
D4
D3
D2
D1
Z score 4
1 s
f
Recorded branch
D1
D2
D3
D4
D5
Stimulated branch
Time (ms)

Figure S14. Correlational structure of spontaneous and opto-evoked dynamics. a, Top: reconstructed dendritic morphology (same neuron as in Fig. 3), showing locations of recorded dendrites. Bottom: top-down view, showing five simultaneously recorded dendritic branches. **b,** Matrix of pairwise contour distances between recorded dendritic segments. **c,** Pair-wise cross correlation matrix of spontaneous activity. Each plot shows the cross-correlation functions of the voltage dynamics in the dendrites from the corresponding row and column. Blue: anesthetized (1% isoflurane); Orange: awake. **d,** Round-robin optogenetic stimulation. Blue light was targeted sequentially to individual dendritic branches, and the voltage responses were recorded in the stimulated branch and all other branches. **e,** Example recording, showing blue light targeted to dendrite D3 evoked local depolarizations. **f,** Stimulus-triggered average membrane depolarizations were calculated for each stimulated branch and each recorded branch. Matrix showing normalized coupling amplitudes between all branch pairs. Line and shading shows mean ± s.e.m. The branch-branch coupling for local opto-stim was smaller than the branch-branch correlations of spontaneous dynamics, suggesting correlated synaptic inputs between branches. Similar results were obtained in n = 4 neurons, 4 mice.

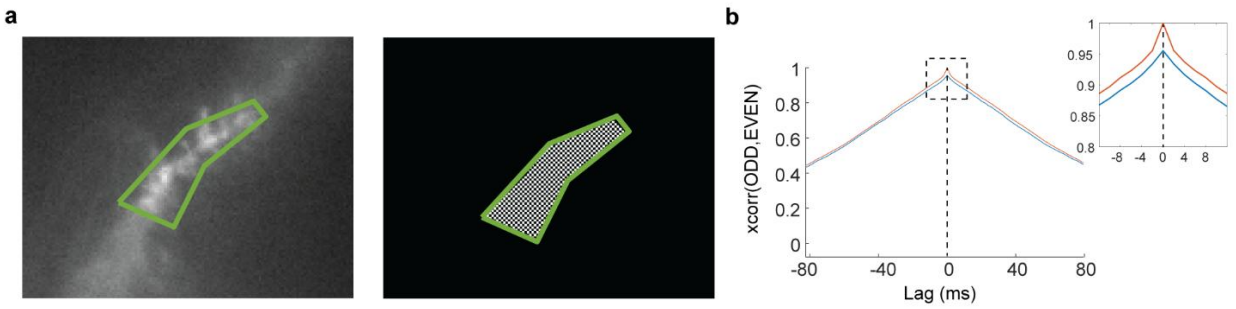

Figure S15. Shot-noise-robust estimates of auto- and cross-correlations. The statistical independence of photon shot-noise at adjacent pixels can be used to estimate auto- and cross-correlations that are not affected by shot noise. **a,** A region of interest (ROI) is defined around each dendritic branch and split into two signals corresponding to the averages of interleaved checkerboard patterns of pixels (i.e. even pixels and odd pixels). These two signals are nearly identical, except for independent realizations of the photon shot noise. **b,** By comparing the autocorrelation of the signal taken from the whole ROI (orange plot) to the cross-correlation of the even- and odd-pixel subregions (blue plot), we determine the contribution of photon shot-noise to the autocorrelation. The cross-correlation between even and odd pixels at zero-lag represents the maximum possible cross-correlation between dendritic branches, taking into account the contribution of shot noise.

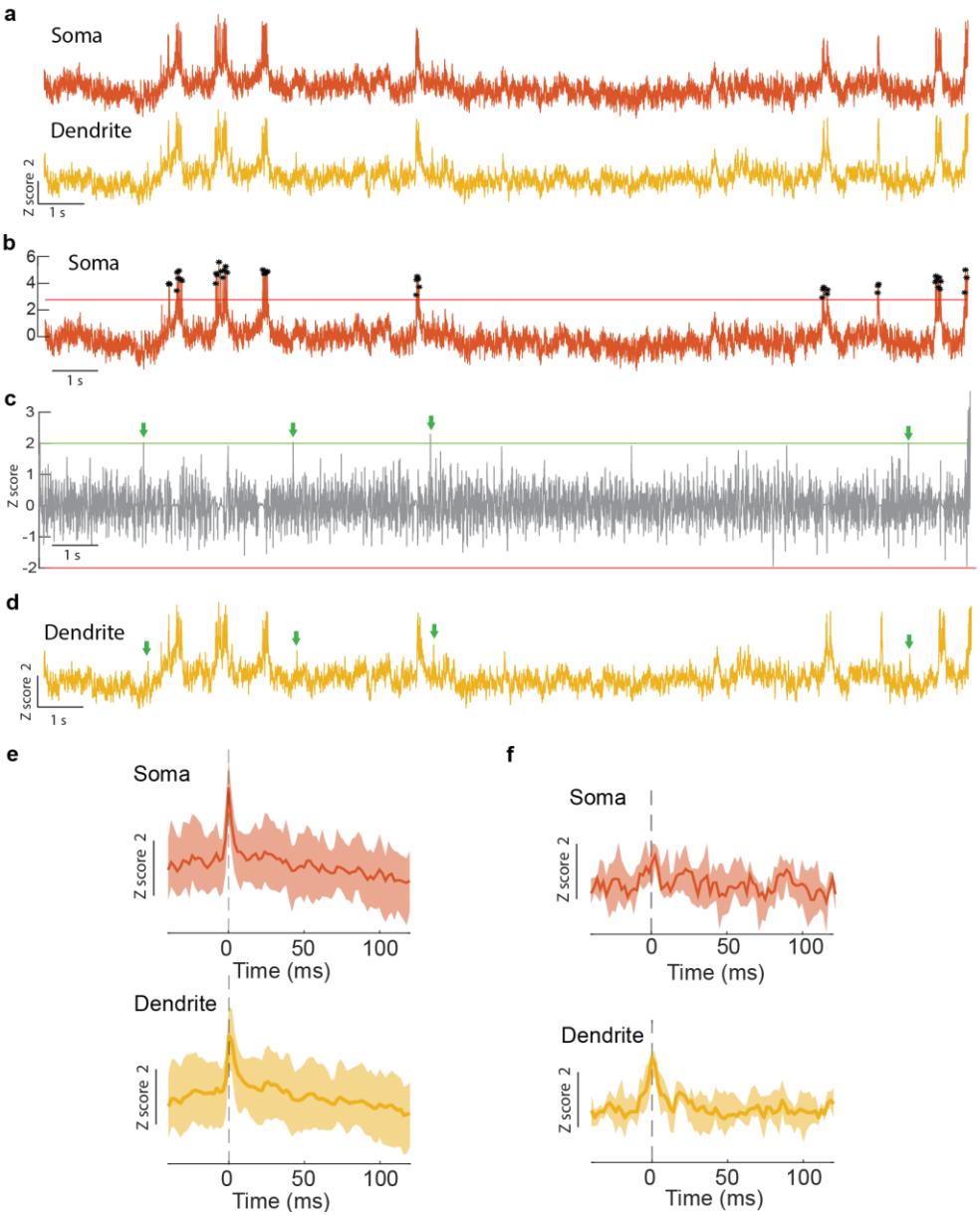

Figure S16. Detecting spikes in the soma and dendrites. a, Traces in each compartment were obtained from the signal-extraction pipeline (**Fig. S8**). **b,** Somatic spike times were defined as the local maximum between upward and downward crossings of a manually defined threshold. The SNR of somatic recordings was typically high enough that the number of detected spikes was not sensitive to the choice of threshold, over a range of visually reasonable threshold values. **c,** To detect dendrite-only events, we digitally removed 10 ms epochs following somatic spikes (to avoid counting bAPs). We then high-pass filtered the dendrite trace by subtracting a median filtered trace with a window width of 50 frames. The spike-detection threshold was set at 2σ (green line). A -2σ threshold (red line) was used to determine the false-positive rate. **d,** Dendritic spike times (green arrows) shown on the original dendritic voltage recording. **e,** Spike triggered average of bAPs on soma and dendrite. **f,** Event-triggered averaged of putative fast dendritic spikes (points in **d**), showing a spike waveform in the dendrite without a corresponding spike at the soma.

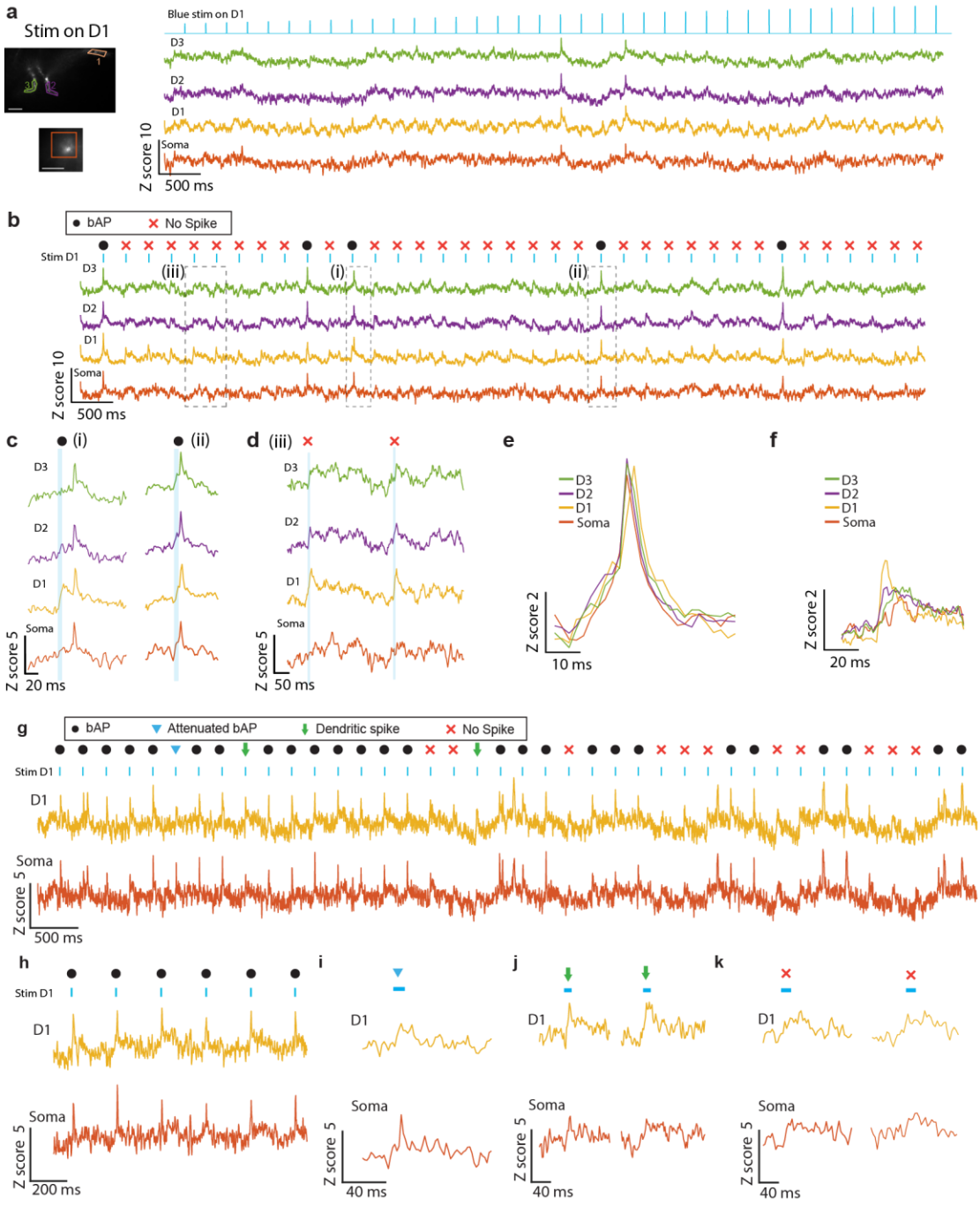

Figure S17. Targeted dendrite stimulation occasionally evokes localized dendritic events. **a,** A single dendritic branch was stimulated at gradually increasing blue intensity (8 ms pulses, 4 Hz, anesthetized mouse) to determine the intensity at which spikes started to appear, i.e. optical rheobase. Scale bars 20 μm. **b,** Dendritic stimuli were targeted to D1, with constant stimulus strength below optical rheobase. Stimuli typically evoked subthreshold depolarizations in D1 only, but sometimes also evoked bAPs. **c,** Examples where optogenetic stimulation of D1 evoked a local subthreshold depolarization and then later a spike at the soma which back-propagated into

D1 and the other branches. **d,** Example where optogenetic stimulation of D1 evoked a local depolarization in D1 but no corresponding event at the soma. Blue bars represent the optogenetic stimulus times. **e-f**, Spike-triggered averages of (e) bAPs (n = 5) and (f) local D1 depolarization events (n = 32). **g,** Example recording with strong dendrite-targeted stimuli (8 ms, 4 Hz). **h,** Examples in which dendrite stimulation evoked spikes at the soma and bAPs in the dendrite. Other rare events comprised: **i,** putative attenuated bAPs; **j,** putative dendritic spikes, comprising depolarization transients detected at the dendrites and not the soma; **k,** subthreshold excitations at dendrite and soma. Recordings were taken at 500 Hz.

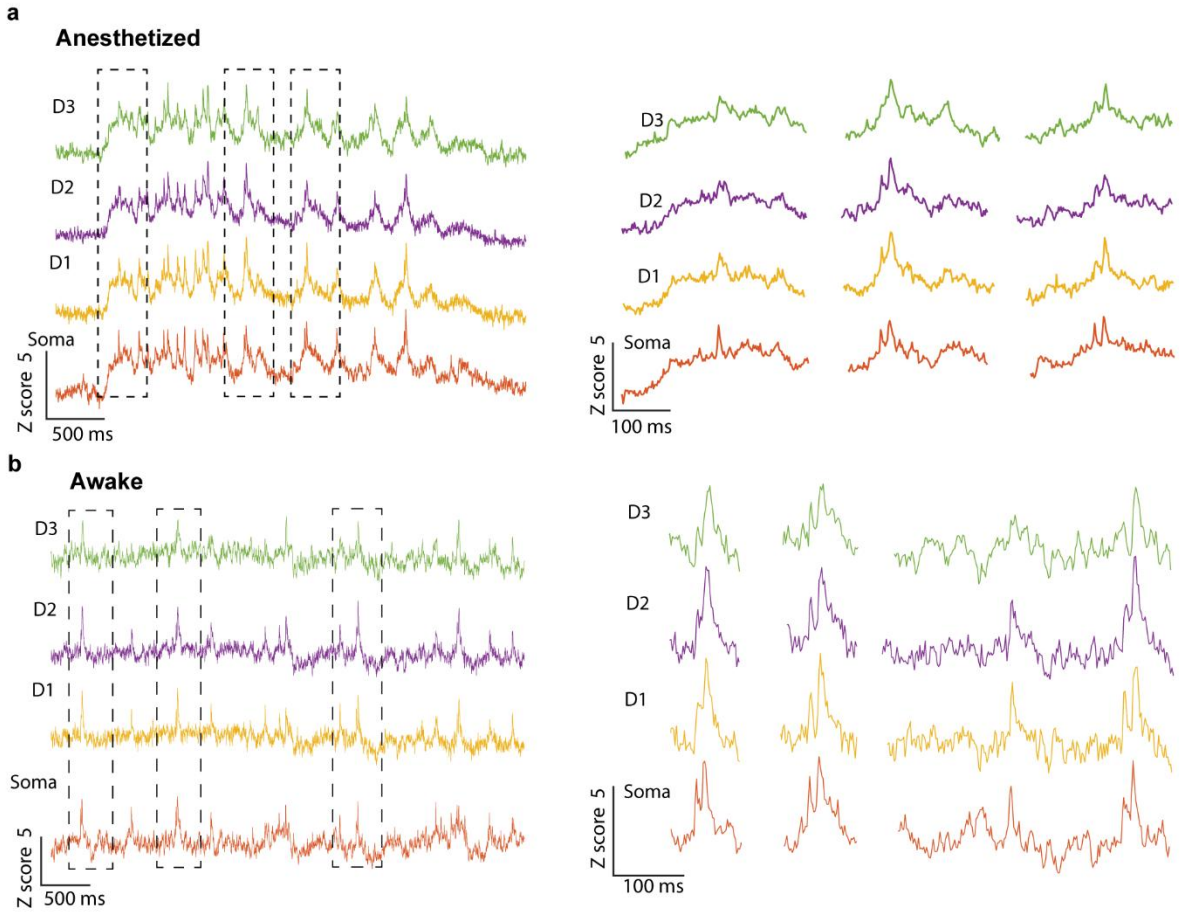

Figure S18. Spontaneous dynamics and attenuated bAP propagation. Example traces of spontaneous activity showing relative bAP attenuation and successful propagation in (**a**) anesthetized and (**b**) awake mouse. The first bAP in a doublet was typically attenuated relative to the second bAP. Rates of attenuated bAPs during anesthesia were very low. Recordings were taken at 500 Hz.

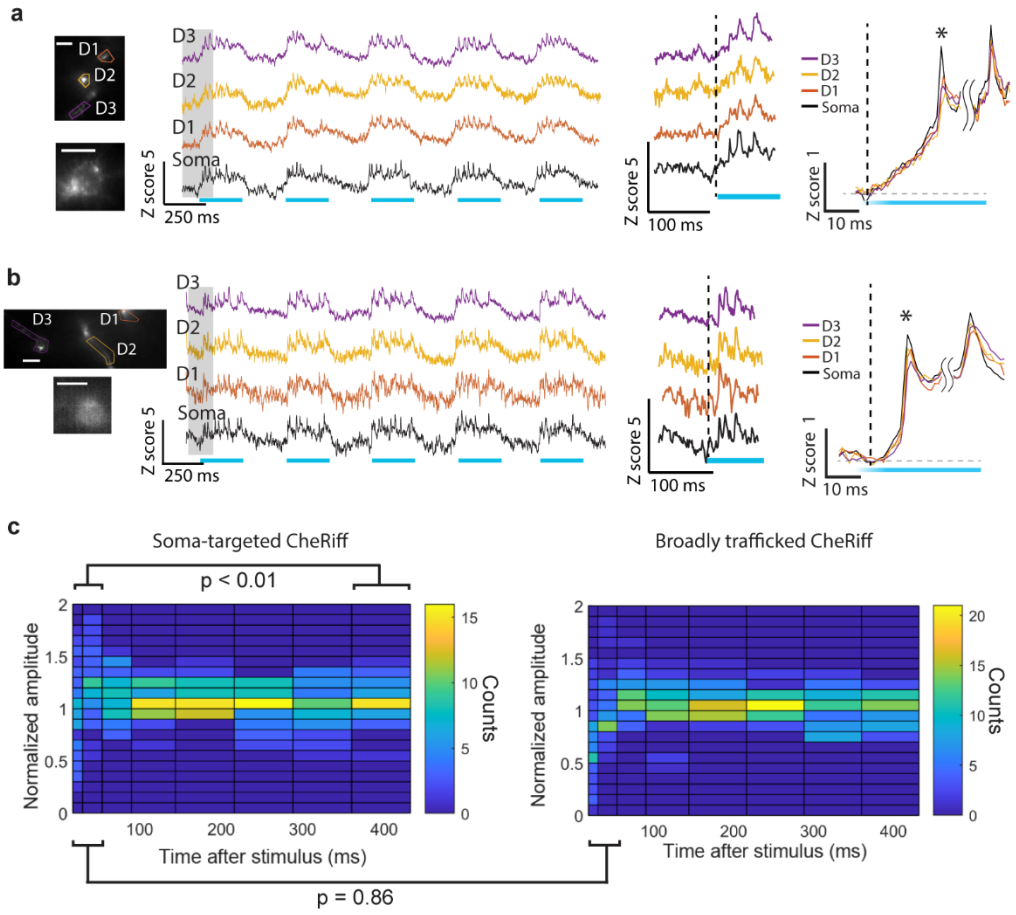

Figure S19. Spike history-dependent back-propagation with soma-targeted opsins. To test whether the spiking history-dependent back-propagation observed in Figs. 4g,h was influenced by optogenetic activation of CheRiff in the dendrites, we repeated the experiment in neurons expressing soma-targeted CheRiff. **a,** Example recordings with optogenetic stimulation and simultaneous voltage imaging in soma and distal dendrites. Scale bars 10 µm. Middle: zoom-in on the onset of the first stimulus pulse (shaded area at left), showing that the first spike was attenuated in the dendrites relative to subsequent spikes. Right: Spike-triggered averages for the first and second spike after stimulus. The precise timing of the first and seconds spikes varied between trials, so the onset of the blue light is shown with a gradient and the time-axis is broken between the events. **b,** Example recordings with a shorter electrotonic distance between the soma and dendrites (as determined by bAP delay times < 3 ms). In these cases there was little history-dependent modulation of bAP amplitude. Scale bars 10 µm. **c,** Histograms of dendritic bAP amplitudes (normalized to amplitude at the soma) vs. time after stimulus onset for the soma-targeted (left) and the broadly trafficked (right) CheRiff expression. In both constructs the initial bAPs were attenuated in the dendrites relative to later bAPs (soma-targeted CheRiff: 173 trials, 29 dendrites, 11 neurons 11 mice; broadly trafficked CheRiff: 187 trials, 22 dendrites, 7 neurons, 7 mice). P values were computed with the two-sided Wilcoxon rank sum test. Recordings were taken at 500 Hz.

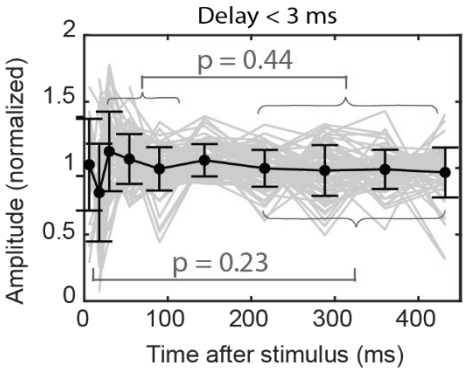

Figure S20. bAPs are neither attenuated nor amplified in proximal dendrites. bAP amplitude in proximal dendrites (defined by peak delay < 3 ms relative to soma) as a function of time after onset of a step-wise optogenetic stimulus (*n* = 30 dendrites, 11 neurons, 11 mice). Neither relative attenuation of the first bAP nor relative amplification of bAPs from 50 – 150 ms were observed (compare to **Fig. 4e-h**). P-values: Two-sided Wilcoxon rank sum test.

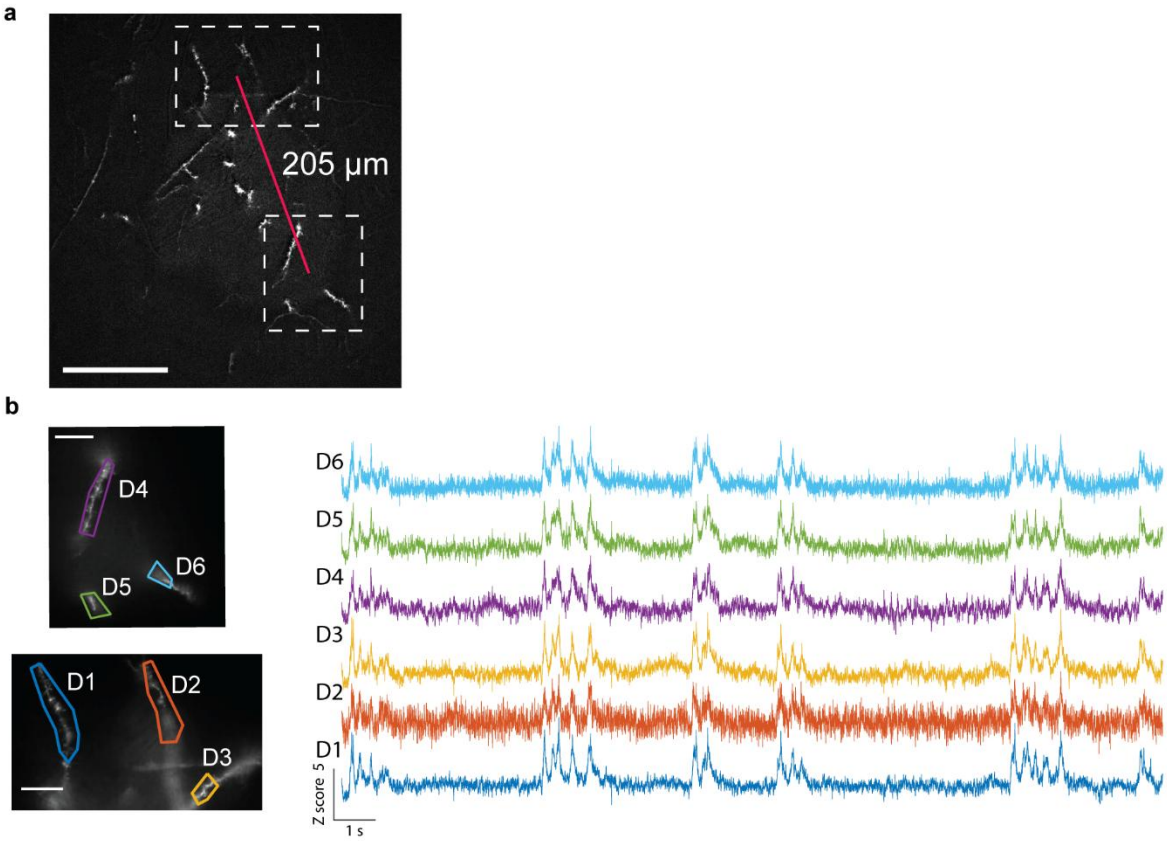

Figure S21. Recording dendritic voltages in two laterally offset fields of view. Independent control of the field of view of each camera allowed simultaneous recording of distant branches from the same neuron. **a,** Wide-area HiLo image of an apical dendrite arbor. The two cameras were set to record from regions separated center-to-center by 205 µm. Scale bar 100 µm. **b,** Individual camera recording fields and single-dendrite regions of interest with example traces from the two fields of view. We observed a high correlation of up-down states across all recorded branches. Scale bars 20 µm. Recordings were taken at 500 Hz.